

Abundance and temperature distributions in the hot intra-cluster gas of Abell 4059

F. Mernier^{1,2}, J. de Plaa¹, L. Lovisari³, C. Pinto⁴, Y.-Y. Zhang³, J. S. Kaastra^{1,2}, N. Werner^{5,6}, and A. Simionescu⁷

¹ SRON Netherlands Institute for Space Research, Sorbonnelaan 2, 3584 CA Utrecht, The Netherlands e-mail: F.Mernier@sron.nl

² Leiden Observatory, Leiden University, P.O. Box 9513, 2300 RA Leiden, The Netherlands

³ Argelander-Institut für Astronomie, Auf dem Hügel 71, D-53121 Bonn, Germany

⁴ Institute of Astronomy, Madingley Road, CB3 0HA Cambridge, United Kingdom

⁵ Kavli Institute for Particle Astrophysics and Cosmology, Stanford University, 452 Lomita Mall, Stanford, CA 94305, USA

⁶ Department of Physics, Stanford University, 382 Via Pueblo Mall, Stanford, CA 94305-4060, USA

⁷ Institute of Space and Astronautical Science (ISAS), JAXA, 3-1-1 Yoshinodai, Chuo-ku, Sagami-hara, Kanagawa, 252-5210 Japan

Received 2014 / Accepted

ABSTRACT

Using the EPIC and RGS data from a deep (200 ks) XMM-Newton observation, we investigate the temperature structure (kT and σ_T) and the abundances of 9 elements (O, Ne, Mg, Si, S, Ar, Ca, Fe and Ni) of the intra-cluster medium (ICM) in the nearby ($z=0.046$) cool-core galaxy cluster Abell 4059. Next to a deep analysis of the cluster core, a careful modelling of the EPIC background allows us to build radial profiles up to $12'$ (~ 650 kpc) from the core. Probably because of projection effects, the temperature ICM is found not to be in single phase, even in the outer parts of the cluster. The abundances of Ne, Si, S, Ar, Ca and Fe, but also O are peaked towards the core. Fe and O are still significantly detected in the outermost annuli; suggesting that the enrichment by both type Ia and core-collapse SNe started in the early stages of the cluster formation. However, the particularly high Ca/Fe ratio that we find in the core is not well reproduced by the standard SNe yield models. Finally, 2-D maps of temperature and Fe abundance are presented and confirms the existence of a denser, colder, and Fe-rich ridge southwest of the core, previously observed by *Chandra*. The origin of this asymmetry in the hot gas of the cluster core is still unclear, but might be explained by a past intense ram-pressure stripping event near the central cD galaxy.

Key words. X-rays: galaxies: clusters – galaxies: clusters: general – galaxies: clusters: intracluster medium – intergalactic medium – galaxies: abundances – galaxies: interactions – supernovae: general

1. Introduction

The deep gravitational potential of clusters of galaxies retains large amounts of hot ($\sim 10^7$ – 10^8 K) gas, mainly visible in X-rays, which accounts for no less than 80% of the total baryonic mass. This so-called intra-cluster medium (ICM) contains not only H and He ions but also heavier metals. Iron (Fe) was discovered in the ICM with the first generation of X-ray satellites (Mitchell et al. 1976); then neon (Ne), magnesium (Mg), silicon (Si), sulfur (S), argon (Ar) and calcium (Ca) were measured with ASCA (e.g. Mushotzky et al. 1996). Precise abundance measurements of these elements have been made possible thanks to the good spectral resolution and the large effective area of the XMM-Newton (Jansen et al. 2001) instruments (e.g. Tamura et al. 2001). Nickel (Ni) abundance measurements and the detection of rare elements like chromium (Cr) have been reported as well (e.g. Werner et al. 2006; Tamura et al. 2009). Finally, due to its low and stable instrumental background, Suzaku is also capable of providing accurate abundance measurements in the cluster outskirts (e.g. Werner et al. 2013).

These metals clearly do not have a primordial origin; they are thought to be mostly produced by supernovae (SNe) within cluster galaxy members and have enriched the ICM mainly around $z \sim 2$ – 3 , i.e. during a peak of the star formation rate (Hopkins & Beacom 2006). However, the respective contributions of the different transport processes required to explain this enrichment

are still under debate. Among them, galactic winds (De Young 1978; Baumgartner & Breitschwerdt 2009) are thought to play the most important role in the ICM enrichment itself. Ram-pressure stripping (Gunn & Gott 1972; Schindler et al. 2005), galaxy-galaxy interactions (Gnedin 1998; Kapferer et al. 2005), AGN outflows (Simionescu et al. 2008, 2009b) and perhaps gas sloshing (Simionescu et al. 2010) can also contribute to the redistribution of elements. Studying the metal distribution in the ICM is a crucial step in order to understand and quantify the role of these mechanisms in the chemical enrichment of clusters.

Another open question is the relative contribution of SNe types producing each chemical element. While O, Ne and Mg are thought to be produced mainly by core-collapse SNe (SNcc, including types Ib, Ic and II, e.g. Nomoto et al. 2006), heavier elements like Ar, Ca, Fe and Ni are probably produced mainly by type Ia SNe (SNIa, e.g. Iwamoto et al. 1999). Si and S are produced by both types (see de Plaa 2013, for a review). The abundances of high-mass elements highly depend on SNIa explosion mechanisms, while the abundances of the low-mass elements (e.g. nitrogen) are sensitive to the stellar initial mass function (IMF). Therefore, measuring accurate abundances in the ICM can help to constrain or even rule out some models and scenarios. Moreover, significant discrepancies exist between recent measurements and expectations from current favoured theoretical yields (e.g. de Plaa et al. 2007), and require thus further investigation.

The temperature distribution in the ICM is often complicated and its underlying physics is not yet fully understood. For instance, many relaxed cluster cores are radiatively cooling on short cosmic timescales, which was presumed to lead to so-called cooling flows (see Fabian 1994 for a review). However, the lack of cool gas (including the associated star formation) in the core revealed in particular by *XMM-Newton* (Peterson et al. 2001; Tamura et al. 2001; Kaastra et al. 2001) leads to the so-called cooling-flow problem and argues for substantial heating mechanisms, yet to be found and understood. For example, heating by AGN could explain the lack of cool gas (see e.g. Cattaneo & Teyssier 2007). Studying the spatial structure of the ICM temperature in galaxy clusters may help to solve it.

Abell 4059 is a good example of a nearby ($z=0.0460$, Reiprich & Böhringer 2002) cool-core cluster. Its central cD galaxy hosts the radio source PKS 2354-35 which exhibits two radio lobes along the galaxy major axis (Taylor et al. 1994). In addition to *ASCA* and *ROSAT* observations (Ohashi 1995; Huang & Sarazin 1998), previous *Chandra* studies (Heinz et al. 2002; Choi et al. 2004; Reynolds et al. 2008) show a ridge of additional X-ray emission located ~ 20 kpc southwest of the core, as well as two X-ray ghost cavities that only partly coincide with the radio lobes. Moreover, the southwest (SW) ridge has been found to be colder, denser, and owning a higher metallicity than the rest of the ICM, suggesting a past merging history of the core prior to the triggering of the AGN activity.

In this paper we analyse in details two deep *XMM-Newton* observations (~ 200 ks in total) of A 4059, obtained through the CHEERS¹ project (de Plaa et al., in prep.). The *XMM-Newton* EPIC (European Photon Imaging Camera) instruments allow us to derive the abundances of O, Ne, Mg, Si, S, Ar, Ca, Fe and Ni not only in the core, but also up to ~ 650 kpc in the outer parts of the ICM. The *XMM-Newton* RGS (Reflection Grating Spectrometer) instruments are also used to measure N, O, Ne, Mg, Si and Fe. This paper is divided as follows: the data reduction is described in Sect. 2. We discuss our selected spectral models as well as our background estimation in Sect. 3. We then present our temperature and abundance measurements in the cluster core, as well as their systematic uncertainties (Sect. 4), measured radial profiles (Sect. 5) and temperature and Fe abundance maps (Sect. 6). We discuss and interpret our results in Sect. 7 and conclude in Sect. 8. Throughout this paper we assume $H_0 = 70 \text{ km s}^{-1} \text{ Mpc}^{-1}$, $\Omega_m = 0.3$ and $\Omega_\Lambda = 0.7$. At the redshift of 0.0460, 1 arcmin corresponds to ~ 54 kpc. The whole EPIC field-of-view (FoV) covers $R \simeq 0.81 \text{ Mpc} \simeq 0.51 r_{200}$ (Reiprich & Böhringer 2002, where r_{200} is the radius within which the density of cluster reaches 200 times the critical density of the Universe). All the abundances are given relative to the proto-solar values from Lodders et al. (2009). The error bars indicate 1σ uncertainties at 68% confidence level. Unless mentioned otherwise, all our spectral analysis is done within 0.3–10 keV by using the Cash statistic (Cash 1979).

2. Observations and data reduction

Two deep observations (DO) of A 4059 were taken on the 11th and 13th May 2013 with a gross exposure time of 96 ks and 95 ks respectively (here after DO #1 & DO #2). In addition to these deep observations, two shorter observations (SO, see also Zhang et al. 2011) are also available from the *XMM-Newton* archive. The observations are summarised in Table 1. Both DO and SO datasets are used for the RGS analysis while for the EPIC analy-

Table 1. Summary of the observations of Abell 4059. We report the total exposure time together with the net exposure time remaining after screening of the flaring background.

| ID | Obs. number | Date | Instrument | Total time (ks) | Net time (ks) |
|-------|-------------|------------|------------|--------------------|------------------|
| SO #1 | 0109950101 | 2000 11 24 | RGS | 29.3 | 20.0 |
| SO #2 | 0109950201 | 2000 11 24 | RGS | 24.7 | 23.4 |
| DO #1 | 0723800901 | 2013 05 11 | EPIC MOS 1 | 96.4 | 71.0 |
| | | | EPIC MOS 2 | 96.4 | 73.0 |
| | | | EPIC pn | 93.8 | 51.7 |
| | | | RGS | 97.1 | 77.1 |
| DO #2 | 0723801001 | 2013 05 13 | EPIC MOS 1 | 94.7 | 76.4 |
| | | | EPIC MOS 2 | 94.7 | 77.5 |
| | | | EPIC pn | 92.9 | 66.4 |
| | | | RGS | 96.1 | 87.9 |

sis we only use the DO datasets. In fact, the SO observations account for $\sim 20\%$ of the total exposure time, and consequently the signal-to-noise ratio S/N would increase only by $\sqrt{1.20} \simeq 1.10$ while the risk of including extra systematic errors and unstable fits due to the EPIC background components (Sect. 3 & Appendix B) is high. The RGS extraction region is small, has a high S/N , and its background modelling is simpler than using EPIC; therefore combining the DO and SO remains safe.

The datasets are reduced using the *XMM-Newton* Science Analysis System (SAS) v13 and partly with the SPEX spectral fitting package (Kaastra et al. 1996) v2.04.

2.1. EPIC

In both DO datasets the MOS and pn instruments were operating in Full Frame mode and Extended Full Frame mode respectively. We reduce MOS 1, MOS 2 and pn data using the SAS tasks *emproc* and *emproc*. Next, we filter our data to exclude soft-proton (SP) flares by building appropriate Good Time Intervals (GTI) files (Appendix A.1) and we excise visible point sources to keep the ICM emission only (Appendix A.2). We keep the single, double, triple and quadruple events in MOS (*pattern* ≤ 12). Due to issues regarding charge transfer inefficiency for the double events in the pn detector², we keep only single events in pn (*pattern* $=0$). We remove out-of-time events from both images and spectra. After the screening process, the EPIC total net exposure time is ~ 150 ks (i.e. $\sim 80\%$ of the initial observing time). In addition to EPIC MOS 1 CCD3 and CCD6 which are not operational anymore, CCD4 shows obvious signs of deterioration, so we discard its events from both datasets as well.

Fig. 1 and 2 show an exposure map corrected combined EPIC image of our full filtered dataset (both detectors cover the full EPIC FoV). The peak of the X-ray emission is seen at $\sim 23^{\text{h}} 57' 0.8''$ RA, $-34^{\circ} 45' 34''$ DEC.

We extract the EPIC spectra of the cluster core from a circular region centred on the X-ray peak emission and with a radius of 3 arcmin (Fig. 2). Using the same center we also extract the spectra of 8 concentric annuli, together covering the FoV within $R \leq 12$ arcmin (Fig. 1). The core region corresponds to the 4 innermost annuli. The RMFs and ARFs are processed using the SAS tasks *rmfgen* and *arfgen* respectively. In order to look at possible substructures in temperature and metallicity, we also create EPIC maps. We divide our EPIC observations in spatial cells using the Weighted Voronoi Tessellations (WVT) adaptive binning algorithm (Diehl & Statler 2006). We restrict the size of our full maps to $R \leq 6$ arcmin. The cell sizes are defined in such

² See the *XMM-Newton* Current Calibration File Release Notes, XMM-CCF-REL-309 (Smith, Guainazzi & Saxton 2014)

¹ CHEmical Evolution Rgs cluster Sample

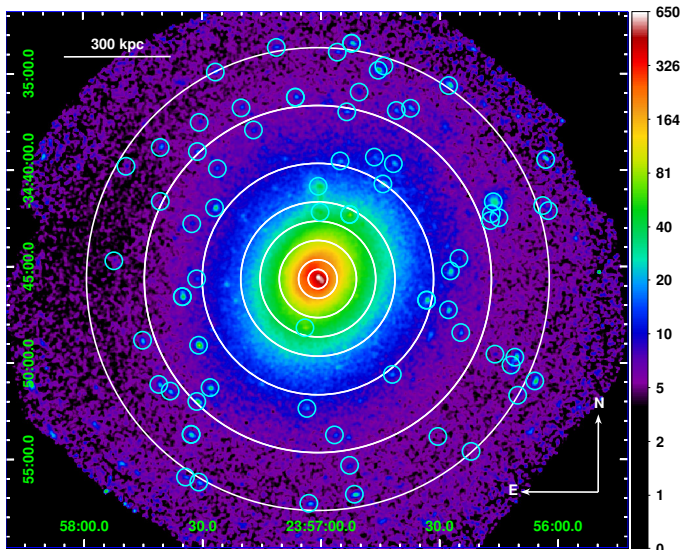


Fig. 1. Exposure map corrected EPIC combined image of A 4059, in units of number of counts. The two datasets have been merged. The cyan circles show the detected resolved point sources that we excise from our analysis. For clarity of display the radii shown here are exaggerated (excision radius = $10''$, see Appendix A.2). The white annuli show the extraction regions that are used for our radial studies (see text & Sect. 5).

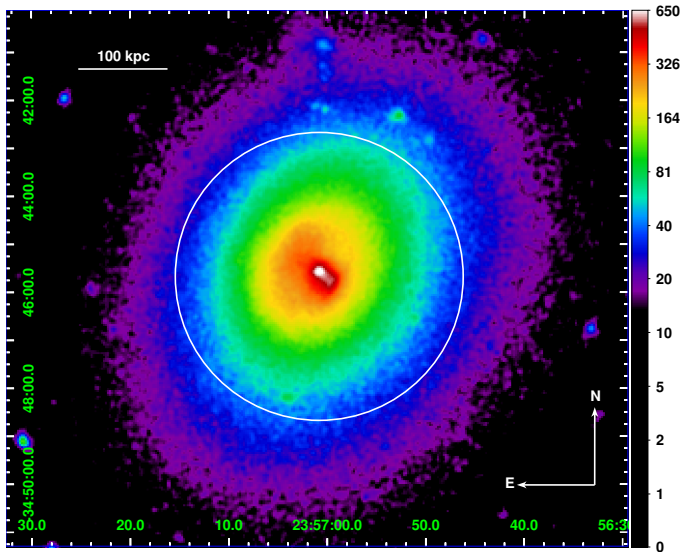


Fig. 2. Close-up view from Fig. 1, centred on the cluster core. The white circle delimitates the core region analysed in Sect. 4.

a way that in every cell $S/N = 100$. The relative errors of the measured temperature and Fe abundance are then expected to be not higher than $\sim 5\%$ and $\sim 20\%$ respectively (see Appendix C for more details). Because SAS does not allow to process RMFs and ARFs for complex geometry regions, we extract them on 10×10 square regions covering together our whole map and we attribute the raw spectra of each cell to the response files of its closest square region. The spectra and response files are converted into SPEX format using the auxiliary program *trafo*.

2.2. RGS

RGS data of all four observations are used (see Table 1 and also Pinto et al. 2014, for details). The RGS detector is centred on the cluster core and its dispersion direction extends to the northeast-southwest direction. We process RGS data with the SAS task *rgsproc*. We correct for contamination from SP flares by using the data from CCD9, where hardly any emission from the source is expected. We build the GTI files similarly to the EPIC analysis (Appendix A.1) and we reprocess the data again with *rgsproc* by filtering the events with these GTI files. The total RGS net exposure time is 208.4 ks. We extract response matrices and RGS spectra for the observations. The final net exposure times are reported in Table 1.

We subtract a model background spectrum created by the standard RGS pipeline from the total spectrum. This is a template background file, based on the count rate in CCD9 of RGS.

We combine the RGS 1 and RGS 2 spectra, responses and background files of the four observations through the SAS task *rgscombine* obtaining one stacked spectrum for spectral order 1 and one for order 2. The two combined spectra are converted to SPEX format through *trafo*. Based on the MOS 1 image, we correct the RGS spectra for instrumental broadening as described in Appendix A.3. We include 95% of the cross-dispersion direction in the spectrum.

3. Spectral models

The spectral analysis is done using SPEX. Since there is an important offset in the pointing of the two observations, stacking the spectra and the response files of each of them may lead to bias in the fittings. Moreover, the remaining SP component is found to change from one observation to another (see Appendix B). Therefore, the better option is to fit simultaneously the single spectra of every EPIC instrument and observation. This has been done using *trafo*.

3.1. CIE

We assume that the ICM is in Collisional Ionization Equilibrium (CIE) and use the *CIE* model in our fits (see the SPEX manual³). Our emission models are corrected from the cosmological redshift and absorbed by the interstellar medium of the Galaxy (for this pointing $N_H \approx 1.26 \times 10^{20} \text{ cm}^{-2}$ as obtained with the method of Willingale et al. 2013). The free parameters in the fits are the emission measure $Y = \int n_e n_H dV$, the (single-) temperature kT , and O, Ne, Mg, Si, S, Ar, Ca, Fe and Ni abundances. The other abundances with an atomic number $Z \geq 6$ are fixed to the Fe value.

3.2. GDEM

Although *CIE* single- (i.e. isothermal) temperature models fit the X-ray spectra from the ICM reasonably well, previous papers (see e.g. Peterson et al. 2003; Kaastra et al. 2004; Werner et al. 2006; de Plaa et al. 2006; Simionescu et al. 2009b) have shown that employing a distribution of temperatures in the models provide significantly better fits, especially in the cluster cores. Indeed, the strong temperature gradient in case of cooling flows and the 2-D projection of the supposed spherical geometry of the ICM suggest that using multi-temperature models would be preferable. Apart from the *CIE* model mentioned above, we also

³ <http://www.sron.nl/spex>

fit a Gaussian Differential Emission Measure (*GDEM*) model to our spectra. This model assumes that the emission measure Y follows a Gaussian temperature distribution centred on kT_{mean} and as defined by:

$$Y(x) = \frac{Y_0}{\sigma_T \sqrt{2\pi}} \exp\left(-\frac{(x - x_{\text{mean}})^2}{2\sigma_T^2}\right) \quad (1)$$

where $x = \log(kT)$ and $x_{\text{mean}} = \log(kT_{\text{mean}})$ (see de Plaa et al. 2006). Compared to the *CIE* model, the additional free parameter from the *GDEM* model is the width of the Gaussian emission measure profile σ_T . By definition $\sigma_T=0$ is the isothermal case.

3.3. Cluster emission and background modelling

We fit the spectra of the cluster emission with a *CIE* and a *GDEM* model successively, except for the EPIC radial profiles and maps, where only a *GDEM* model is considered.

Since the EPIC cameras are highly sensitive to the particle background, a precise estimate of the local background is crucial in order to estimate ICM parameters beyond the core (i.e. where this background is comparable to the cluster emission). The emission of A 4059 fills entirely the EPIC FoV, making a direct measure of the local background impossible. Some efforts have been done in the past to deal with this issue (see e.g. Zhang et al. 2009, 2011; Snowden & Kuntz 2013), but a customised procedure based on full modelling is more convenient in our case. In fact, a wrong subtraction of instrumental fluorescence lines might lead to wrong abundance estimates.

For each extraction region, several background components are modelled in the EPIC spectra in addition to the cluster emission. This modelling procedure as well as its application to our extracted regions are fully described in Appendix B. Note that unlike in EPIC, we do not explicitly model the cosmic X-ray background in RGS because any diffuse emission feature would be smeared out into a broad continuum-like component.

4. Cluster core

4.1. EPIC

Our deep exposure time allows us to get precise abundance measurements in the core, even using EPIC (Fig. 3 left). Moreover, the background is very limited since the cluster emission clearly dominates. Table 2 shows our results, both for the combined (MOS+pn) and independent (either MOS or pn only) fits.

Using a multi-temperature model clearly improves the combined MOS+pn fit. Nevertheless, even by using a *GDEM* model, the reduced C-stat value is still high because the excellent statistics of our data reveal anti-correlated residuals between MOS and pn, especially below ~ 1 keV (Fig. 3 right).

When we fit the EPIC instruments independently, the reduced C-stat number decreases from 1.87 to 1.40 and 1.78 in the MOS and pn fits respectively. Visually, the models reproduce better the spectra as well. We also note that the temperature and abundances measurements in the core are different between the instruments (Table 2). While temperature discrepancies between MOS and pn have been already reported and investigated (Schellenberger et al. 2014), here we focus on the MOS-pn abundance discrepancies. Fig. 4 (left) illustrates them and shows the absolute abundance measurements obtained from our *GDEM* models. Except for Ne, Ar and Ca (all consistent within 2σ), we observe systematically higher values in MOS than in pn. Assuming (at least for convenience) that the systematic errors are

roughly Gaussian distributed, we can estimate them for different abundance measurements Z_{MOS} and Z_{pn} , having their respective statistical errors σ_{MOS} and σ_{pn} :

$$\sigma_{\text{sys}} = \sqrt{\sigma_{\text{tot}}^2 - \frac{\sigma_{\text{MOS}}^2 + \sigma_{\text{pn}}^2}{2}} \quad (2)$$

where $\sigma_{\text{tot}} = \sqrt{((Z_{\text{MOS}} - \mu)^2 + (Z_{\text{pn}} - \mu)^2)/2}$ and $\mu = (Z_{\text{MOS}} + Z_{\text{pn}})/2$. We obtain absolute O, Si, S and Fe systematic errors of $\pm 25\%$, $\pm 30\%$, $\pm 34\%$ and $\pm 14\%$ respectively. The MOS-pn discrepancies in Mg and Ni are too big to be estimated as reasonable systematic errors (Fig. 4). No systematic errors are necessary for the absolute abundances of Ne, Ar and Ca.

If we normalise the abundances relative to Fe in each instrument (Fig. 4 right panel), O/Fe is consistent within 2σ and Si/Fe and S/Fe within 3σ . Inversely, the discrepancies on Ar/Fe measurements slightly increase, but their statistical uncertainties are quite large because its main line (~ 3.1 keV) is weak. Note that the discrepancies in Mg and Ni measurements remain huge and almost unchanged. Based on the same method as above, we find that systematic errors of O/Fe, Si/Fe and S/Fe are reduced to $\pm 8\%$, $\pm 15\%$ and $\pm 20\%$ while the systematic errors of Ar/Fe increase to $\pm 27\%$.

4.1.1. Equivalent widths

One way of determining the origin of the discrepancies in the fitted abundance from different instruments is to derive the abundances using a more robust approach. Instead of fitting the abundances using the *GDEM* model directly, we model each main emission line/complex by a Gaussian and a local continuum (hereafter the 'Gauss' method). The *GDEM* model is still used to fit the local continuum; however only the Fe abundance is kept to its best-fit value, the other abundances are set to zero⁴. We then check the consistency of this method by comparing it with the abundances reported above (hereafter the 'GDEM' method) in terms of equivalent width (EW), which we define for each line as

$$\text{EW} = \frac{F_{\text{line}}}{F_c(E)} \quad (3)$$

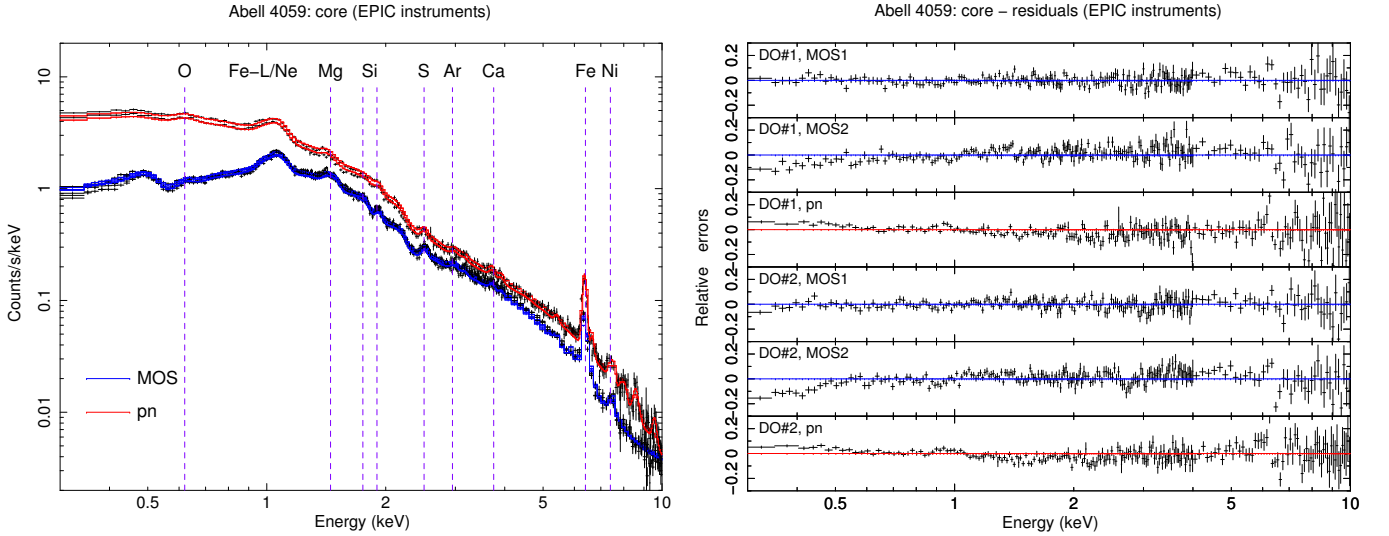
where F_{line} and $F_c(E)$ are the fluxes of the line and the continuum at the line energy E respectively. Since the EW of a line is proportional to the abundance of its ion, in principle both methods should yield the same abundance. We compare them on the strongest lines of Mg, Si, S, Ca, Fe and Ni in MOS and pn spectra (Table 3) and we convert the average MOS+pn EWs into abundance measurements (Fig. 4). While we find consistency between the 'Gauss' and 'GDEM' methods for Ca and Fe-K lines both in MOS and pn, the other elements need to be further discussed.

The EW of Mg obtained in pn using the 'Gauss' method is significantly ~ 9 times higher than using the 'GDEM' method. In the latter case, the pn continuum of the model is largely overestimated around ~ 1.5 keV, making the Mg abundance underestimated. Si and S also show significantly larger EWs in pn using the 'Gauss' method. In terms of abundance measurements, they both agree with the MOS measurements (Fig. 4). Also note that beyond ~ 1.5 keV the MOS residuals ratio are known to be significantly higher than the pn ones (Read et al. 2014), and peak

⁴ When fitting the Fe-K line, obviously the Fe abundance is also set to zero.

Table 2. Best-fit parameters measured in the cluster core (circular region, $R \sim 3$ arcmin). A single-temperature (*CIE*) and a multi-temperature (*GDEM*) models have been successively fitted.

| Parameter | Model | MOS+pn | MOS only | pn only |
|----------------------------------|-------------|-------------------|-------------------|-------------------|
| C-stat / d.o.f. | <i>CIE</i> | 3719/1781 | 1904/1221 | 1109/546 |
| | <i>GDEM</i> | 3331/1780 | 1703/1220 | 969/545 |
| Y (10^{70} m^{-3}) | <i>CIE</i> | 806 ± 3 | 779.7 ± 1.8 | 827 ± 3 |
| | <i>GDEM</i> | 821 ± 3 | 792 ± 3 | 845 ± 4 |
| kT (keV) | <i>CIE</i> | 3.696 ± 0.012 | 3.837 ± 0.015 | 3.431 ± 0.18 |
| kT_{mean} (keV) | <i>GDEM</i> | 3.838 ± 0.016 | 4.03 ± 0.02 | 3.58 ± 0.03 |
| σ_T | | 0.261 ± 0.004 | 0.266 ± 0.007 | 0.251 ± 0.008 |
| O | <i>CIE</i> | 0.49 ± 0.03 | 0.57 ± 0.04 | 0.34 ± 0.03 |
| | <i>GDEM</i> | 0.46 ± 0.04 | 0.57 ± 0.04 | 0.33 ± 0.04 |
| Ne | <i>CIE</i> | 1.08 ± 0.04 | 1.09 ± 0.04 | 1.05 ± 0.05 |
| | <i>GDEM</i> | 0.33 ± 0.05 | 0.34 ± 0.06 | 0.36 ± 0.08 |
| Mg | <i>CIE</i> | 0.45 ± 0.04 | 0.82 ± 0.05 | < 0.04 |
| | <i>GDEM</i> | 0.45 ± 0.03 | 0.78 ± 0.05 | < 0.08 |
| Si | <i>CIE</i> | 0.49 ± 0.02 | 0.64 ± 0.03 | 0.32 ± 0.03 |
| | <i>GDEM</i> | 0.51 ± 0.02 | 0.66 ± 0.03 | 0.35 ± 0.03 |
| S | <i>CIE</i> | 0.46 ± 0.03 | 0.61 ± 0.04 | 0.25 ± 0.05 |
| | <i>GDEM</i> | 0.52 ± 0.03 | 0.66 ± 0.04 | 0.31 ± 0.05 |
| Ar | <i>CIE</i> | 0.27 ± 0.07 | 0.17 ± 0.15 | 0.35 ± 0.14 |
| | <i>GDEM</i> | 0.41 ± 0.08 | 0.30 ± 0.11 | 0.54 ± 0.15 |
| Ca | <i>CIE</i> | 0.89 ± 0.09 | 0.91 ± 0.11 | 0.78 ± 0.15 |
| | <i>GDEM</i> | 1.01 ± 0.10 | 0.98 ± 0.13 | 0.90 ± 0.15 |
| Fe | <i>CIE</i> | 0.740 ± 0.008 | 0.851 ± 0.009 | 0.624 ± 0.009 |
| | <i>GDEM</i> | 0.697 ± 0.006 | 0.803 ± 0.010 | 0.600 ± 0.010 |
| Ni | <i>CIE</i> | 1.04 ± 0.08 | 1.86 ± 0.11 | 0.34 ± 0.11 |
| | <i>GDEM</i> | 1.04 ± 0.07 | 1.83 ± 0.11 | 0.37 ± 0.10 |

**Fig. 3.** EPIC spectra (left) and residuals (right) of the core region ($0'-3'$) of Abell 4059. The two observations are displayed and fitted simultaneously with a *GDEM* model. For clarity of display the data are rebinned above 4 keV by a factor of 10 and 20 in MOS and pn spectra respectively.

near the Si line. This might also partly explain the discrepancies found for S, Si and maybe Mg.

When using the 'GDEM' method for pn, the Ni-K line is poorly fitted. The large difference in EW obtained when fitting it using the 'Gauss' method also emphasises this effect. In fact, when fitting the pn spectra using a *CIE* or *GDEM* model, a low Ni abundance is computed by the model to compensate the issues in the calibration of the effective area around 1.0–1.5 keV (i.e. where most Ni-L lines are present). For this reason and large error bars of the Ni-K line, the fit in pn ignores it.

If we fit the spectra between 2–10 keV only (after having frozen kT , σ_T , O, Mg and Si obtained in our previous fits), we obtain Ni abundances of 1.61 ± 0.35 and 1.37 ± 0.26 for MOS and pn respectively, making them consistent between each other. This clearly favours the Ni abundance measured with MOS in our previous fits. Interestingly, we also measure Fe abundances of 0.752 ± 0.019 and 0.676 ± 0.017 for MOS and pn respectively; their discrepancies are then reduced but still remain. Finally note that the pn data are shifted by ~ 20 eV compared to the model around the Fe-K line; this shift does not affect the abundance measurements though.

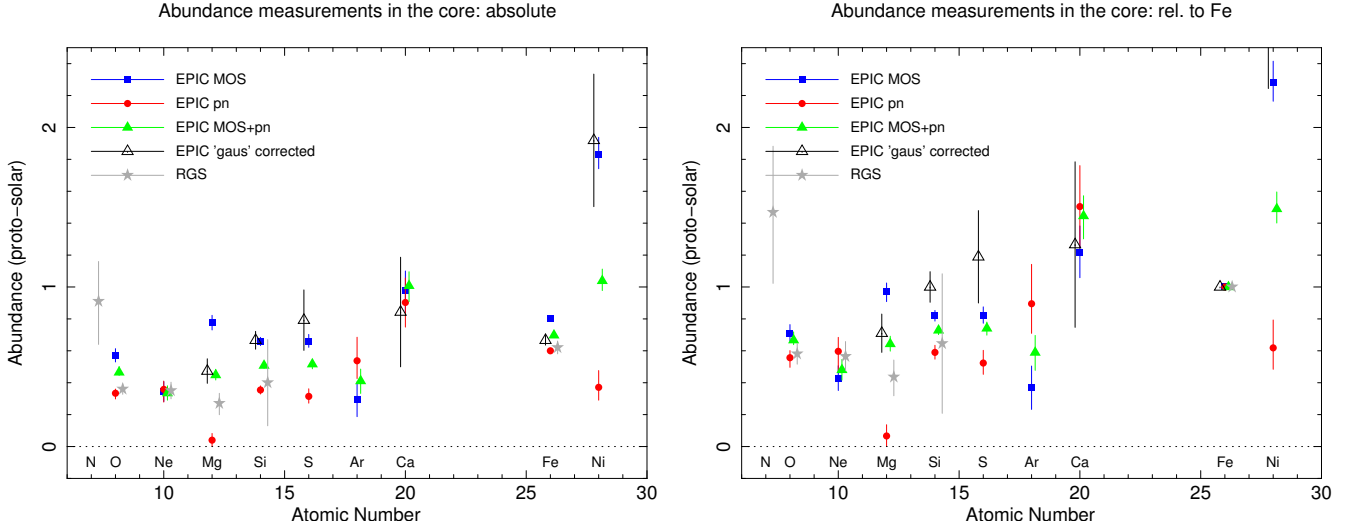


Fig. 4. EPIC and RGS abundance measurements in the core of A 4059. Left: absolute abundances. Right: Abundances relative to Fe. The black empty triangles show the mean MOS+pn abundances obtained by fitting Gaussian lines instead of the CIE models ('Gauss' method; see text and Table 3). The numerical values are summarized in Table 4.

Table 3. Measured equivalent widths of K-shell lines in the core (0'–3') using the 'Gauss' and 'GDEM' methods for MOS and pn independently.

| Elem. | Line E (keV) | MOS | | pn | |
|-------|-----------------|----------------------------|-----------------------------|----------------------------|-----------------------------|
| | | EW _{GDEM} (eV) | EW _{Gauss} (eV) | EW _{GDEM} (eV) | EW _{Gauss} (eV) |
| Mg | 1.44 | 13.8±0.9 | 10.1±1.2 | 0.8±0.8 | 7.5±1.7 |
| Si | 2.00 | 36.8±1.7 | 41 ±3 | 24 ±2 | 41 ±4 |
| S | 2.62 | 39 ±2 | 61 ±12 | 23 ±4 | 41 ±13 |
| Ca | 3.89 | 30 ±4 | 25 ±11 | 33 ±5 | 32 ±12 |
| Fe | 6.65 | 820±10 | 776±34 | 684±11 | 652±32 |
| Ni | 7.78 | 127±8 | 182±33 | 28 ±8 | 92 ±26 |

Table 4. Summary of the absolute abundances measured in the core (EPIC and RGS) using a *GDEM* model. The mean MOS+pn abundances obtained by fitting Gaussian lines instead of the CIE models ('Gauss' method; see text and Table 3) is also included. See also Fig. 4.

| Elem. | EPIC | | | | RGS |
|-------|-------------|-------------|-------------|---------------|-----------|
| | MOS | pn | MOS+pn | 'Gauss' corr. | |
| N | – | – | – | – | 0.9±0.3 |
| O | 0.57±0.04 | 0.33±0.04 | 0.46±0.04 | – | 0.36±0.03 |
| Ne | 0.34±0.06 | 0.36±0.08 | 0.33±0.05 | – | 0.35±0.05 |
| Mg | 0.78±0.05 | < 0.08 | 0.45±0.03 | 0.47±0.08 | 0.27±0.07 |
| Si | 0.66±0.03 | 0.35±0.03 | 0.51±0.02 | 0.67±0.06 | 0.4±0.3 |
| S | 0.66±0.04 | 0.31±0.05 | 0.52±0.03 | 0.79±0.19 | – |
| Ar | 0.30±0.11 | 0.54±0.15 | 0.41±0.08 | – | – |
| Ca | 0.98±0.13 | 0.90±0.15 | 1.01±0.10 | 0.8±0.3 | – |
| Fe | 0.803±0.010 | 0.600±0.010 | 0.697±0.006 | 0.67±0.03 | 0.62±0.04 |
| Ni | 1.83±0.11 | 0.37±0.10 | 1.04±0.07 | 1.9±0.4 | – |

Our results on the abundance analysis in the core are summarised in Table 4 and Fig. 4 and are briefly discussed in Sect. 7.1. Because of their too large uncertainties, we choose not to consider Mg and Ni abundances in the rest of the paper. Moreover, although the MOS-pn discrepancies are sometimes big and make some absolute abundance measurements quite uncertain, in the following sections we are most interested in their spatial variations. By comparing combined *MOS+pn* measurements only, the systematic errors we have shown here should not play an important role in this purpose.

Table 5. RGS spectral fits of Abell 4059.

| Parameter | 1-T <i>CIE</i> | 2-T <i>CIE</i> | <i>GDEM</i> |
|------------------------------------|----------------|----------------|-------------|
| C-stat/d.o.f. | 1274/887 | 1244/886 | 1268/885 |
| Y_1 (10^{70} m^{-3}) | 683±4 | 662±6 | 480±8 |
| T_1 (keV) | 2.74±0.08 | 2.8±0.1 | – |
| Y_2 (10^{70} m^{-3}) | – | 4 ±1 | – |
| T_2 (keV) | – | 0.80±0.07 | – |
| T_{mean} (keV) | – | – | 3.4±0.2 |
| σ_T | – | – | 0.26±0.03 |
| N | 0.7±0.2 | 0.9±0.3 | 0.9±0.3 |
| O | 0.32±0.03 | 0.35±0.03 | 0.36±0.03 |
| Ne | 0.40±0.05 | 0.43±0.06 | 0.35±0.05 |
| Mg | 0.26±0.06 | 0.32±0.07 | 0.27±0.07 |
| Si | 0.6±0.3 | 0.8±0.3 | 0.4±0.3 |
| Fe | 0.57±0.03 | 0.63±0.04 | 0.62±0.04 |

4.2. RGS

Our RGS analysis of the core region focuses on the 7–28 Å (0.44–1.77 keV) first and second order spectra of the RGS detector. RGS stacked spectra are binned by a factor of 5. We test single-, two-temperature *CIE* models, and a *GDEM* model for comparison.

The models are redshifted and, to model the absorption, multiplied by a *hot* model (i.e. an absorption model where the gas is assumed to be in CIE) with a total $N_H = 1.26 \times 10^{20} \text{ cm}^{-2}$ (Willingale et al. 2013), $kT = 0.5 \text{ eV}$ and proto-solar abundances.

In order to take into account the emission-line broadening due to the spatial extent of the source, we have convolved the emission components by the *lpro* multiplicative model in SPEX (Tamura et al. 2004; Pinto et al. 2014).

The RGS order 1 and 2 stacked spectra have been fitted simultaneously (Fig. 5) and the results of the spectral fits are shown in Table 5 and Fig. 4. The 2-T *CIE* and *GDEM* fits are comparable in terms of Cash statistics and the models are visually similar. Although there might be some residual emission at temperature below 1 keV that can be reproduced by the 2-T *CIE* model (Frank et al. 2013), using a *GDEM* model is more realistic regarding temperature distribution found in the core of most

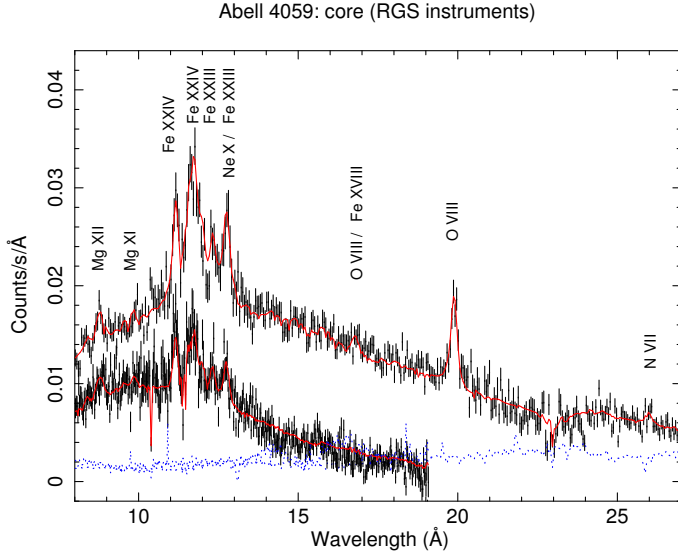


Fig. 5. RGS first and second order spectra of A 4059 (see also Table 5). The spectra are fitted with a 2-T *CIE* model. The subtracted backgrounds are shown in blue dotted lines. The main resolved emission lines are also indicated.

clusters. The abundances are in agreement between the different models because they depend on the relative strength of the lines.

5. EPIC radial profiles

We fit the EPIC spectra from each of the 8 annular regions mentioned in Sect. 2 using a *GDEM* model. We derive projected radial profiles of the temperature, temperature broadening and abundances (Table 6). In our measurements, all the cluster parameters (Y , kT , σ_T and abundances) are coupled between the three instruments and the two datasets. Since we ignore the channels below 0.4 keV (MOS) and 0.6 keV (pn) in the outermost annulus to avoid background contamination (Appendix B), we restrict our O radial profile within 9'. For the same reason, the O abundance measurement between 6'–9' might be biased up to ~ 25% (i.e. our presumed MOS-pn systematic uncertainty for the O measurement).

In order to quantify the trends that appear in our profiles, we fit them with simple empirical distributions. For temperature and abundance profiles,

$$kT(r) = D_\infty + \alpha \exp(-r/r_0) \quad (4)$$

$$Z(r) = D_\infty + \alpha \exp(-r/r_0) \quad (5)$$

and for σ_T radial profile,

$$\sigma_T(r) = D_\infty + \alpha r^\gamma. \quad (6)$$

Table 7 shows the results of our fitted trends. Fig. 6 shows the radial profiles and their respective best-fit distributions.

The temperature profile reveals a significant drop from ~2.5' to the innermost annuli, confirming the presence of a cool-core. Beyond ~2.5', the temperature stabilises around $kT \sim 4.2$ keV. More surprisingly, after a plateau around 0.22 from the core to ~2.5', σ_T increases up to 0.33 ± 0.04 in the outermost annulus. This increase is also significant in our best-fit distribution. In this outer region, we show that kT and σ_T are slightly correlated

Table 7. Best-fit parameters of empirical models for our radial profiles. For the meaning of α , r_0 , γ and D_∞ , see Eqs. 4, 5 and 6 in the text. Unless mentioned (^{CIE}), the empirical models follow the *GDEM* measurements of Table 6.

| Param. | α | r_0 | γ | D_∞ | $\chi^2/\text{d.o.f.}$ |
|--------------------------|-------------------|----------------------|---------------|-------------------|------------------------|
| kT_{mean} | -1.66 ± 0.04 | 1.21 ± 0.08 | — | 4.22 ± 0.04 | 17.28/4 |
| σ_T | 0.009 ± 0.010 | — | 1.2 ± 0.3 | 0.220 ± 0.016 | 3.79/4 |
| kT^{CIE} | -1.61 ± 0.04 | 1.04 ± 0.07 | — | 4.05 ± 0.03 | 22.11/4 |
| O | 0.29 ± 0.07 | $1.76^{+1.1}_{-0.4}$ | — | 0.31 ± 0.03 | 7.75/3 |
| O | — | — | — | 0.41 ± 0.02 | 14.22/5 |
| Ne | 0.74 ± 0.12 | 1.63 ± 0.3 | — | < 0.019 | 4.88/4 |
| Si | 0.83 ± 0.03 | 2.83 ± 0.2 | — | < 0.02 | 7.28/4 |
| S | 0.75 ± 0.06 | 3.3 ± 0.6 | — | < 0.02 | 11.72/4 |
| Ar | 0.84 ± 0.18 | $2.5^{+1.0}_{-0.6}$ | — | < 0.07 | 3.52/4 |
| Ar | — | — | — | 0.25 ± 0.04 | 26.52/6 |
| Ca | 1.43 ± 0.3 | $1.5^{+1.6}_{-0.4}$ | — | < 0.64 | 2.24/4 |
| Ca | — | — | — | 0.96 ± 0.13 | 22.12/6 |
| Fe | 0.80 ± 0.02 | 2.96 ± 0.3 | — | 0.14 ± 0.03 | 9.01/4 |
| Fe^{CIE} | 0.82 ± 0.03 | 3.06 ± 0.3 | — | 0.18 ± 0.03 | 11.39/4 |

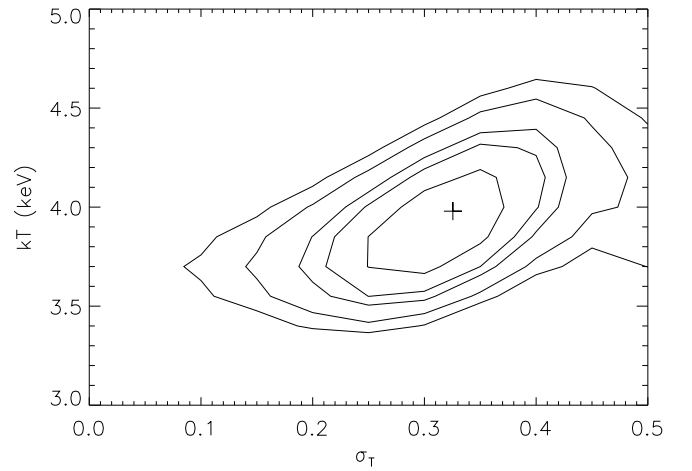


Fig. 7. Error ellipses comparing the temperature kT with the broadening of the temperature distribution σ_T in the 9'–12' annulus spectra. Contours are drawn for 1, 2, 3, 4 and 5 σ . The "+" sign shows the best-fit value.

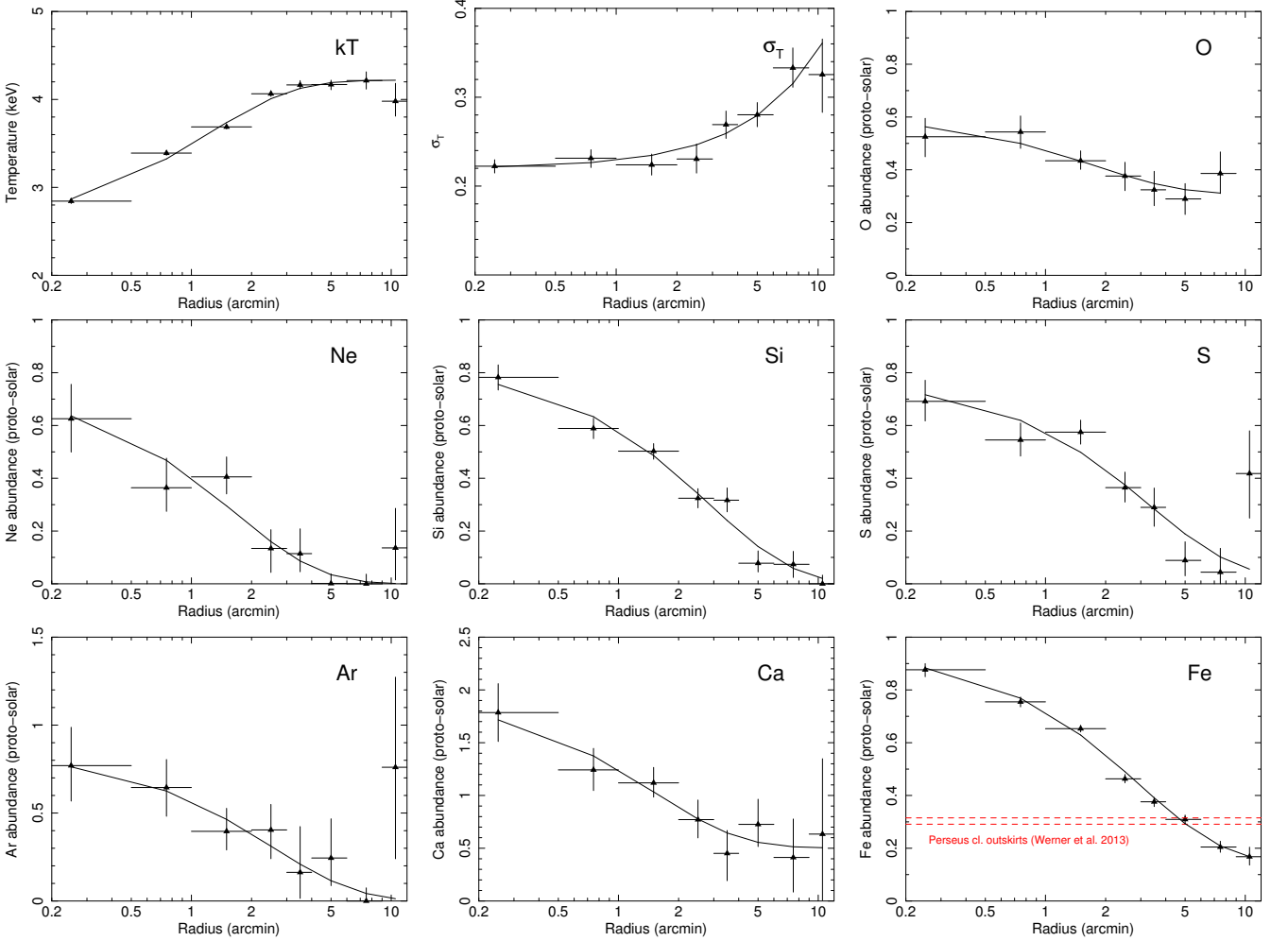
(Fig. 7); however the radial profiles of kT and σ_T show different trends. Moreover, constraining $\sigma_T=0$ in the outermost annulus clearly worsens the goodness of the fit (Fig. 7), meaning that the σ_T increase is probably genuine.

Our analysis reveals a slightly decreasing O radial profile. Even if fully excluding a flat trend is hard based on our data, the exponential model (Eq. 5) gives a better fit than a constant model $Z(r) = D_\infty$ (Table 7). A decrease from 0.54 ± 0.06 to 0.29 ± 0.06 is observed between 0.5'–6' as well. Finally, O is still strongly detected in the outermost annuli. Note however that additional uncertainties should be taken into account (see also above). In fact, the O measurement near the edge of the FoV may also be slightly affected by the modelling of the Local Hot Bubble (Appendix B) through its flux and its assumed O abundance.

As mentioned earlier, Ne is hard to constrain but is detected. Its abundance drops to zero outside the core while it is found to be more than half its proto-solar value within 0.5 arcmin. Profiles of Si and S abundances also decrease, typically from ~0.8 to very low values in the outermost annuli. In every annulus the Si and S measurements are quite similar; this is also confirmed by the best-fit trends which exhibit consistent parameters between the two profiles. The Ar radial profile is harder to interpret be-

Table 6. Best-fit parameters measured in 8 concentric annuli (covering together ~ 12 arcmin of FoV). The spectra of every annulus have been fitted using a *GDEM* model and adapted from our background procedure.

| Parameter | 0' – 0.5' | 0.5' – 1' | 1' – 2' | 2' – 3' | 3' – 4' | 4' – 6' | 6' – 9' | 9' – 12' |
|----------------------------------|-------------------|-------------------|-------------------|-----------------|-----------------|-------------------|-----------------|-----------------|
| C-stat/d.o.f. | 2440/1482 | 2302/1575 | 2641/1670 | 2182/1658 | 1967/1627 | 2061/1703 | 2129/1686 | 2223/1671 |
| Y (10^{70} m^{-3}) | 82.5 ± 0.9 | 155.9 ± 1.2 | 314.0 ± 1.6 | 240.5 ± 1.5 | 176.1 ± 1.1 | 256.7 ± 1.9 | 240 ± 3 | 150 ± 3 |
| kT_{mean} (keV) | 2.84 ± 0.03 | 3.39 ± 0.03 | 3.69 ± 0.02 | 4.06 ± 0.03 | 4.16 ± 0.05 | 4.17 ± 0.06 | 4.21 ± 0.10 | 3.98 ± 0.20 |
| σ_T | 0.222 ± 0.008 | 0.231 ± 0.010 | 0.224 ± 0.012 | 0.23 ± 0.02 | 0.27 ± 0.02 | 0.280 ± 0.014 | 0.33 ± 0.02 | 0.33 ± 0.04 |
| O | 0.53 ± 0.08 | 0.54 ± 0.06 | 0.43 ± 0.04 | 0.38 ± 0.06 | 0.32 ± 0.07 | 0.29 ± 0.06 | 0.39 ± 0.08 | – |
| Ne | 0.63 ± 0.13 | 0.36 ± 0.11 | 0.41 ± 0.08 | 0.14 ± 0.09 | 0.11 ± 0.09 | < 0.04 | < 0.04 | < 0.29 |
| Mg | 0.51 ± 0.09 | 0.51 ± 0.07 | 0.44 ± 0.05 | 0.42 ± 0.07 | 0.45 ± 0.09 | 0.23 ± 0.08 | 0.18 ± 0.10 | < 0.34 |
| Si | 0.78 ± 0.05 | 0.59 ± 0.04 | 0.50 ± 0.03 | 0.32 ± 0.04 | 0.32 ± 0.05 | 0.08 ± 0.05 | 0.07 ± 0.05 | < 0.03 |
| S | 0.69 ± 0.08 | 0.55 ± 0.06 | 0.57 ± 0.05 | 0.36 ± 0.06 | 0.29 ± 0.07 | 0.09 ± 0.07 | < 0.13 | 0.41 ± 0.17 |
| Ar | 0.8 ± 0.2 | 0.65 ± 0.16 | 0.40 ± 0.13 | 0.40 ± 0.16 | < 0.42 | 0.2 ± 0.2 | < 0.07 | 0.8 ± 0.5 |
| Ca | 1.8 ± 0.3 | 1.2 ± 0.2 | 1.12 ± 0.15 | 0.77 ± 0.19 | 0.5 ± 0.3 | 0.7 ± 0.2 | 0.41 ± 0.36 | < 1.34 |
| Fe | 0.88 ± 0.03 | 0.75 ± 0.02 | 0.653 ± 0.013 | 0.46 ± 0.02 | 0.38 ± 0.02 | 0.31 ± 0.02 | 0.20 ± 0.02 | 0.17 ± 0.04 |
| Ni | 1.11 ± 0.17 | 1.28 ± 0.14 | 0.97 ± 0.12 | 0.72 ± 0.15 | 0.68 ± 0.18 | 0.27 ± 0.18 | < 0.25 | < 0.07 |

**Fig. 6.** EPIC radial profiles of Abell 4059. The datapoints show our best-fit measurements (Table 6). The solid lines show our best-fit empirical distributions (Table 7). The spectra of every annulus have been fitted using a *GDEM* model and adapted from our background modelling. Note the change of abundance scale for Ar and Ca.

cause of its large uncertainties, but the trend suggests the same decreasing profile as observed for Si and S.

The Ca radial profile shows particularly high abundances in general, significantly peaked toward the core where it reaches 1.8 ± 0.3 times the proto-solar value and 2.0 ± 0.3 times the local Fe abundance. Finally we show that Fe abundance is also signifi-

cantly peaked within the core and decreases toward the outskirts, where our fitted model suggests a flattening to 0.14 ± 0.03 .

Note that our radial analysis focuses on the projected profiles only. Although deprojection can give a rough idea about the 3-D behaviour of the radial profiles, they are based on the assumption of a spherical symmetry, which is far from being the case in the innermost parts of A 4059 (Sect. 6). Moreover, the deprojected

abundance radial profiles are thought not to deviate significantly from the projected ones (see e.g. Werner et al. 2006). Based on the analysis of Kaastra et al. (2004), we estimate that the contamination of photons into incorrect annuli due to the EPIC point-spread function (PSF) changes our Fe abundance measurements in the order of $\sim 2\%$ and $\sim 4\%$ in the first and second innermost annuli respectively, which is not significant regarding our 1σ error bars. The choice of a *GDEM* model should take into account both the multi-temperature features due to projection effects and the possible PSF contamination in the kT radial profile.

6. Temperature, σ_T and Fe abundance maps

Using a *GDEM* model, we derive temperature and abundance maps from the EPIC data of our two deep observations. The long net exposure time (~ 140 ks) for A 4059 allows to map the distribution of kT , σ_T and Fe abundance within $6'$. Like for the radial analysis all the EPIC instruments and the two datasets are fitted simultaneously.

In order to emphasise the impact of the statistical errors on the maps and to possibly reveal substructures, we create so-called residuals maps following the method of Lovisari et al. (2011). In each cell, we subtract from each measured parameter the respective value estimated from our modelled radial profile (Fig. 6) at the distance r of the geometric centre of the cell. The significance index is defined as being this difference divided by the error on the measured parameter. The kT , σ_T and Fe abundance maps and their respective error and residuals maps are shown in Fig. 8.

The kT map reveals the cool core of the cluster in detail. It appears to be asymmetric and to have a roughly conic shape extending from the north to the east and pointing toward the SW direction. Along this axis, the temperature gradient is steeper to SW than to northeast (NE) of the core. Most of the relative errors obtained with the *CIE* model (not shown here) are within 2–5%, which is in agreement with our expectations (Appendix C); however they slightly increase with radius. This trend is stronger when using the *GDEM* model, and the errors are somewhat larger. A very local part (~ 5 cells) of the core is up to 8σ cooler than our modelled temperature profile. This coldest part is offset $\sim 25''$ SW from the X-ray peak emission. This contrasts with the western part of the core, which shows a significantly hotter bow than the average $\sim 55''$ away from the X-ray peak emission. Also note that some outer cells are found significantly ($>2\sigma$) colder or hotter than the radial trend.

The σ_T map confirms the positive σ_T measurements in most of the cells outside the core, typically within 0.1–0.4. Globally, σ_T is consistent with that measured from the σ_T radial profile. Note that outside the core the errors are quite inhomogeneous and sometimes hard to estimate precisely.

The Fe map also shows that the core is asymmetric. Like in the kT map, the abundance gradient from the core toward the SW direction is steeper than toward the NE direction. The highest Fe emitting region is found to be $\sim 25''$ SW offset from the X-ray peak emission and coincides with the coldest region. In this offset SW region, Fe is measured to be more than 7σ overabundant.

Note that the smallest cells ($\sim 12''$) have a size comparable to the EPIC PSF ($\sim 6''$ FWHM); a contamination from leaking photons between adjacent cells might thus slightly affect our mapping analysis. However, the PSF has a smoothing effect on the spatial distributions, and gradients may be only stronger than they actually show in the map. This does not affect our conclu-

sion of important asymmetries of temperature and Fe abundance in the core of A 4059.

7. Discussion

We determined the temperature distribution and the elemental abundances of O, Ne, Si, S, Ar, Ca and Fe in the core region ($\leq 3'$) of A 4059 and in 8 concentric annuli centred on the core. In addition, we built 2-D maps of the mean temperature (kT), the temperature broadening (σ_T) and the Fe abundance. Due to large cross-calibration uncertainties, Mg and Ni abundances are not reliable in these datasets using EPIC, and we will prefer measure the Mg abundance using RGS instead.

7.1. Abundance uncertainties and SNe yields

As shown in Table 2, the Ne abundance measured using EPIC depends a lot on the choice of the modelled temperature distribution. The main Ne lines are hidden in the Fe-L complex, around ~ 1 keV. This complex contains a lot of strong Fe lines and is extremely sensitive to the temperature. A slight change in the temperature distribution will thus importantly affect the Ne abundance measurement, making it not very reliable using EPIC (see also Werner et al. 2006). For the same reason, Fe abundances of single- and multi-temperature models might change slightly but already cause a significant difference between both models.

Most of the discrepancies in the abundance determination between the EPIC instruments are coming from a wrong estimation of the lines and/or the continuum in pn (Sect. 4.1). Cross-calibration issues between MOS and pn have been already reported (see e.g. de Plaa et al. 2007; Schellenberger et al. 2014), but their deterioration has probably increased over time despite current calibration efforts (Read et al. 2014). Our analysis using the 'Gauss' method (Table 3 & Fig. 4) suggests that in general MOS is more reliable than pn in our case, even though MOS might slightly overestimate some elements as well (e.g. Mg, S or even Fe). In any case, this latest method is the most robust one to estimate the abundances in the core using EPIC.

Another interesting result is our detection of very high Ca/Fe abundances in the core. de Plaa et al. (2006) already reported such a trend in Sérsic 159-03 (de Plaa et al. 2007, see also). Within $0.5'$ the combined EPIC measurements give a Ca/Fe ratio of 2.0 ± 0.3 . This is even higher than measured within $3'$ (Ca/Fe = 1.45 ± 0.14). Following the approach of de Plaa et al. (2007) and assuming a Salpeter IMF, we select different SNIa models (soft deflagration versus delayed-detonation, Iwamoto et al. 1999) as well as different initial metallicities affecting the yields from SNcc population (Nomoto et al. 2006). We fit the constructed SNe models to our measured abundances in the core (O, Ne, Mg and Si from RGS; Ar and Ca from EPIC; Fe from the 'Gauss' method). We find that a WDD2 model, taken with $Z=0.02$ and a Salpeter IMF, reproduce our measurements best, with $(\chi^2/\text{d.o.f.})_{\text{WDD2}} = 4.28/6$ (Fig. 9). Although the fit is reasonable in terms of reduced χ^2 , it is unable to explain the high Ca/Fe value that we found. de Plaa et al. (2007) also considered a delayed-detonation model that fitted the Tycho SNIa remnant best (Badenes et al. 2006). The fit is improved $((\chi^2/\text{d.o.f.})_{\text{Tycho}} = 1.77/5)$, but the model barely reaches the lower error bar of our measured Ca/Fe. Assuming the problem is not fully solved even using the latest model, we can raise two further hypotheses that might explain it:

1. Ca abundance measurements might suffer from additional systematic uncertainties. Our analysis (Sect. 4.1 & 5) shows

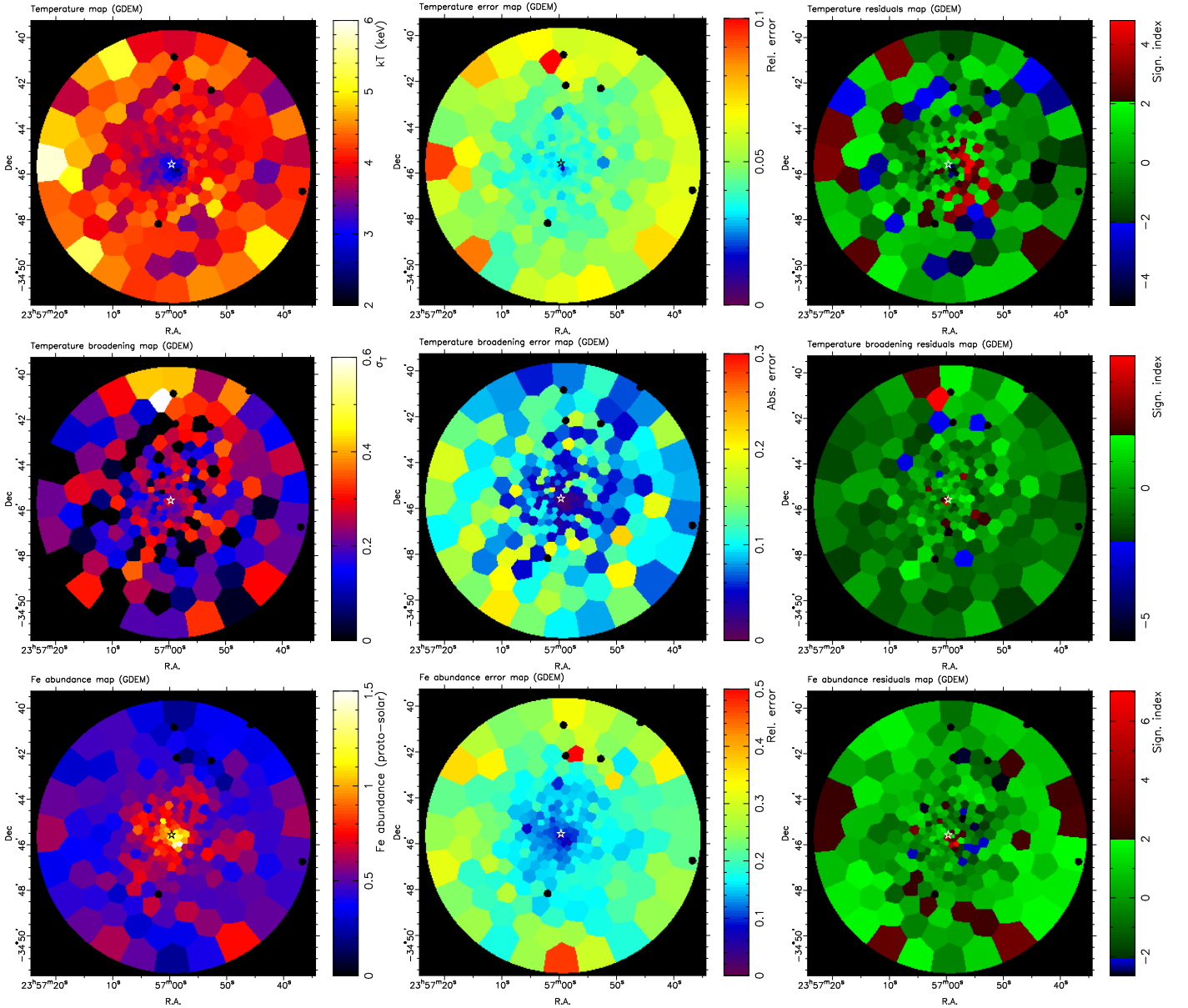


Fig. 8. From upper to lower panels: kT , σ_T and Fe abundance maps of A 4059. The left panels show the basic maps (using a GDEM model). The middle panels show their corresponding absolute ($\Delta\sigma_T$) or relative ($\Delta T/T$; $\Delta Fe/Fe$) errors. The right panels show their corresponding residuals (see text). In the centre of each map, the (black or white) star shows the peak of X-ray emission. All the maps cover $R \leq 6$ arcmin of FoV.

however that MOS and pn Ca/Fe measurements are consistent within the entire core ($3'$). Moreover the continuum and EW of Ca lines (~ 3.9 keV) are correctly estimated by our CIE models. Because of current efforts to limit them, uncertainties in the atomic database could contribute only partly. Finally the effective area at the position of this line is smooth and no instrumental-line feature line is known around ~ 3.9 keV.

2. Some SNe subclasses, so far ignored, might contribute to the metal enrichment in the ICM. For example, the so-called 'calcium-rich gap transients' as a possible subclass of SNIa, are expected to produce a large amount of Ca even outside galaxies, making the transportation of Ca in the ICM much easier (Mulchaey et al. 2014).

7.2. Abundance radial profiles

All the abundance radial profiles decrease with radius. Interestingly, O shows a slight decrease (confirmed by our empirical fitted distribution), even though a flat profile cannot be fully excluded. This decreasing trend has been observed in other clusters, such as Hydra A (Simionescu et al. 2009a), A2029 and Centaurus (Lovisari et al. 2011). However the observations of A 496 (Lovisari et al. 2011) and A 1060 (Sato et al. 2007) suggest a flatter profile. The O distribution is less clear in S3rsic 159-03 (de Plaa et al. 2006; Lovisari et al. 2011).

Moreover, only O and Fe profiles show abundances significantly higher than zero in the outermost annuli. The Fe profile is clearly peaked to the core, and agrees with typical slopes found in many other clusters (e.g. Simionescu et al. 2009a; Lovisari et al. 2011). Moreover, its apparent plateau in the outer regions may suggest a constant Fe abundance in the ICM even outside r_{500} , as recently observed by *Suzaku* in Perseus (Werner

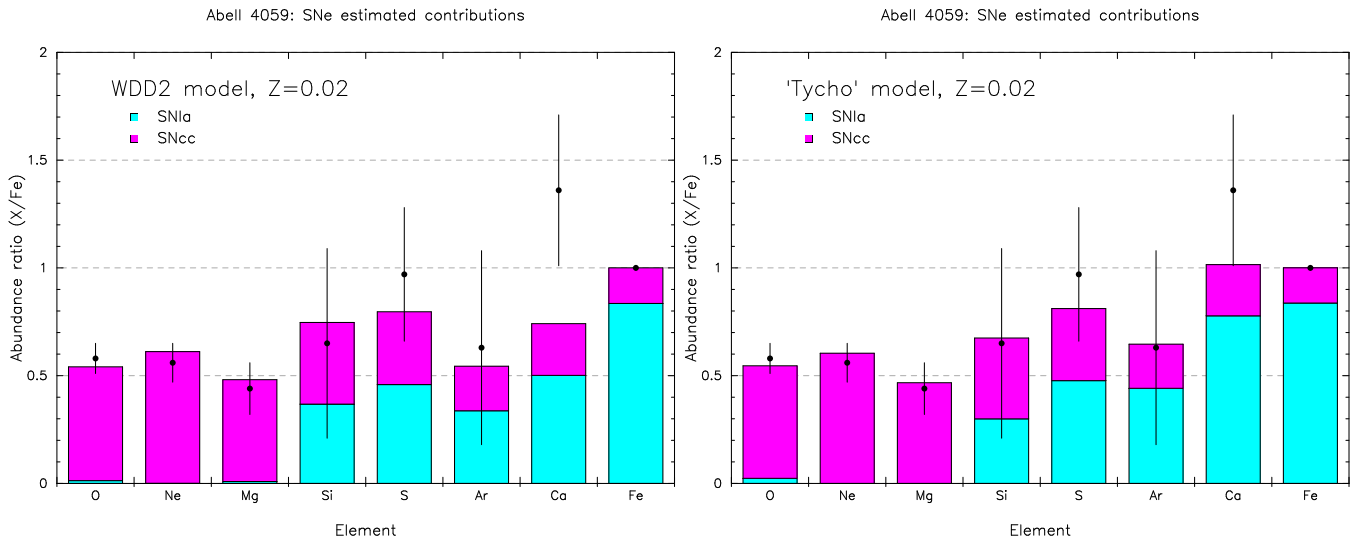


Fig. 9. Comparison of our EPIC abundance measurements with standard SNe yield models. Left panel: WDD2 delayed-detonation SNIa model (Iwamoto et al. 1999). Right panel: empirically modified delayed detonation SNIa model from the yields of the Tycho supernova (Badenes et al. 2006). The two models are computed with a Salpeter IMF and an initial metallicity of $Z = 0.02$ (Nomoto et al. 2006).

et al. 2013) and other clusters (e.g. Leccardi & Molendi 2008; Matsushita 2011). As seen on Fig. 6, the Fe abundance found in the outskirts of Perseus (0.303 ± 0.012 , in proto-solar abundance units) is higher than what we find for A4059, even when accounting for the systematic uncertainties estimated from the core in Sect. 4.1. This constant Fe abundance found in other cluster outskirts and this work suggest that the bulk of the enrichment at least by SNIa started in the early stages of the cluster formation.

In the previous cluster analyses where O appeared to be flat, the increase of O/Fe with radius is usually justified by arguing a very early population of SNIa and SNcc, starting after an intense star formation around $z \sim 2-3$ (Hopkins & Beacom 2006) and undergoing a very efficient mixing all over the potential well, followed by a delayed population of SNIa responsible for the Fe peaked profile, and produced preferably in the central galaxy members in which a strong ram-pressure stripping is assumed (see also discussion for Sérsic 159-03 from de Plaa et al. 2006). Ram-pressure stripping was also suggested to mimic the Fe peak profile between $z = 1$ and $z = 0$ (Schindler et al. 2005). However, De Grandi et al. (2014) suggest that the bulk of the Fe peak was already in place before $z = 1$ in most clusters, meaning that at least SNIa type products started to get a centrally peaked distribution early on in the cluster formation. In fact, Fe seems to follow the near-infrared light profile of the central cD galaxies much better at $z = 1$ than at $z = 0$, suggesting that most of the current mixing mechanisms tend to spread out the metals in the ICM.

The decreasing O radial profile measured in this work suggests that the same kind of scenario is likely for SNcc type products. Although its best-fit slope of the profile appears to be flatter than the slope of the Fe radial profile (Table 7), the O/Fe radial values are still compatible with a constant distribution (except possibly for the $6'-9'$ annulus, where systematics might affect the O measurements). Consequently, a delayed population of SNIa and/or SNcc occurring after $z = 1$ is not necessary to invoke, although it might contribute to a minor part of the metals found in the core. At $z \sim 2-3$ the central cD galaxy and its surrounding galaxy members were already star-forming active and could have produced the bulk of all metals observed in the core, probably injected into the ICM through galactic winds. More recently, ram-pressure stripping could have played a minor role as

well in the enrichment of the core, e.g. to explain the asymmetry found on the maps (see below).

Assuming a flat and positive distribution of Fe and O beyond the FoV, the mixing of the metals is likely very efficient in the outskirts, where the entropy is high. In the core however, the entropy was already very stratified early on without any major mergers to disturb it, and the mixing mechanisms could be less efficient there.

While O and Fe are detected far from the core and favours for an early initial enrichment from SNIa and SNcc types, puzzlingly we do not detect significant abundances of Ne and Si in the outermost annuli. This result is less striking in the S and Ar radial measurements, even though our fitted trends give small upper limits for D_{∞} . Nevertheless, abundance measurement in the outer parts of the FoV can also suffer from additional systematic uncertainties related to the background contribution. These uncertainties may explain our lack of clear detection of Ne, Si, S and Ar in the outermost annuli. Finally, note the similarity between the Si and S profiles, already reported in the cD galaxy M87 by Million et al. (2011).

Beside these radial trends, our maps show local regions of anomalously rich Fe abundance in the core. This is particularly striking in the SW ridge, where the Fe abundance is $> 7\sigma$ higher than the average trend from its corresponding radial profile. Since no galaxy can be associated to this particular region, it is hard to explain its enrichment with galactic winds. As previously reported and discussed by Reynolds et al. (2008), it is possible that an important part of the metals in the core comes from one early starburst galaxy that passed very close to the cD central galaxy before the onset of the central AGN. In this case ram-pressure stripping probably have played a dominant role in the enrichment within ~ 0.5 arcmin after the initial enrichment seen through the radial profiles. This possible scenario is also discussed in the next section.

7.3. Temperature structures and asymmetries

Although the ICM appears well homogeneous and symmetric at large scale, the inner part appears to be more asymmetric (Fig. 2). As already observed in the past by *Chandra* (Heinz et al.

2002; Reynolds et al. 2008), the SW ridge is clearly visible as an additional peaked X-ray emission near the core, and a diffuse tail from the core toward NE can be also detected.

Evidence of asymmetries are also found in our spectral analyses. Although our radial kT profile looks similar to other cool-core clusters, our kT and Fe abundance maps show clear inhomogeneities in the ICM structure of A 4059. Compared to the 2-D maps previously measured using *Chandra* (Reynolds et al. 2008), the S/N of the cells in our EPIC maps are ~ 3.3 and ~ 2.5 times greater for kT and the Fe abundance respectively, allowing us to confirm these substructures with a higher precision and over a larger FoV.

First, like the Fe abundance, the temperature gradient is steeper within the SW ridge than NE of the core. The central core (including the SW ridge) is also significantly colder (~ 2.3 keV) and the SW ridge has a higher Fe abundance (~ 1.5) than the rest of the core within $0.5'$. These results confirm the previous study by Reynolds et al. (2008) who also found strong asymmetry in the core of A 4059 using *Chandra*. Their pressure map shows neither asymmetry nor discontinuity in the core, even around the SW ridge. From both *Chandra* and XMM-Newton studies, it is clear that this ridge plays a role in the metal enrichment of the core (see also Sect. 7.2) and must be closely linked to the history of the cluster (Reynolds et al. 2008). The hotter bow region found W of the core is likely related to it. Based on the *Chandra* images (Reynolds et al. 2008), sloshing seems unlikely to explain the origin of the ridge. Indeed, it appears to be a second brightness peak separated from the core, and its particular morphology is very different from the typical spiral regular pattern of sloshing fronts (see e.g. Paterno-Mahler et al. 2013; Ichinohe et al. 2014). Another scenario is that a local cool, dense and Fe-rich asymmetry was already present before the triggering of central AGN radio-activity, and has been formed by a gas-rich late-type galaxy that plunged very close to the central cD galaxy, there underwent an intense starburst due to its interactions with the dense local ICM and lost an important part of its metals due to the strong gravitational interaction coupled with intense ram-pressure stripping.

Reynolds et al. (2008) estimated that such a galaxy should be within $300v_3$ kpc of the cluster core. They suggested the bright spiral galaxy ESO 349-G009 as being a good candidate, although they were not sure whether this object belongs to A 4059. Looking at the caustic taken from Zhang et al. (2011, see individual galaxy redshifts in the references therein, e.g. Andernach et al. 2005), we can confirm that it is indeed the case (Fig. 10). The galaxy is located in the front part of the cluster and moves with a high radial velocity compared to the cD galaxy ($\Delta v \simeq 1800$ km/s). Assuming that this scenario is correct and that the movement of this galaxy near the central cD galaxy was essentially along the line-of-sight, the absence of an obvious metal tail from ram-pressure stripping on the plane of the FoV becomes naturally explained. Moreover, the X-ray isophotes joining ESO 349-G009 and the cluster ICM (Fig. 11) show an interaction between both and might suggest that the galaxy is escaping from the core. The UV light detected in its arms using the XMM-Newton OM instrument (e.g. UVM2 filter) reveals that the galaxy still has a high star formation rate. The gas mass of the ridge ($5 \times 10^9 M_\odot$) is about a few percent of the total stellar mass of ESO 349-G009 (Reynolds et al. 2008).

Finally, both the radial profile and map reveal a constant or increasing trend of σ_T with radius. This is likely explained by projection effects such as the increased effective length along our line of sight. For cooling core clusters, this effective length increases as a function of radius, and a longer effective length

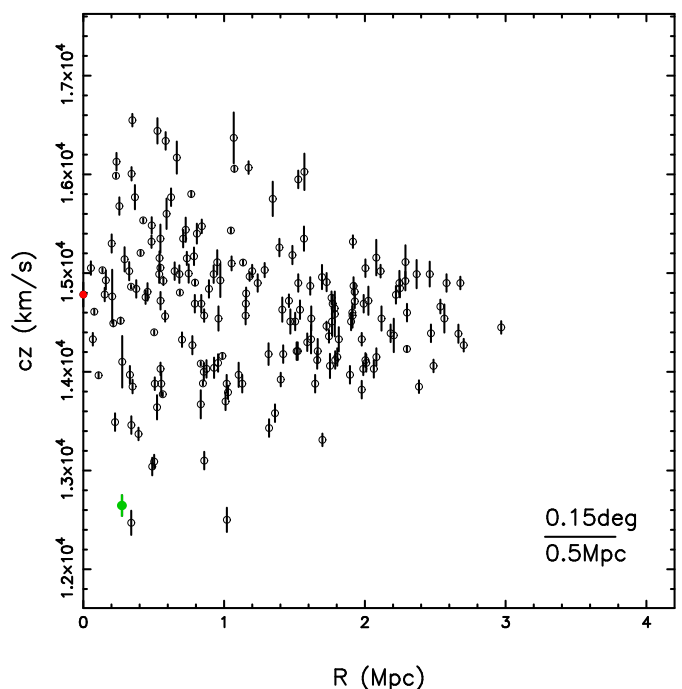


Fig. 10. Line-of-sight velocity versus projected distance from the central cD galaxy for the member galaxies with optical spectroscopic redshifts in A 4059 taken from Zhang et al. (2011). The central cD galaxy is shown in red. The location of spiral galaxy ESO 349-G009 (green) in the caustic indicates that it belongs to the cluster.

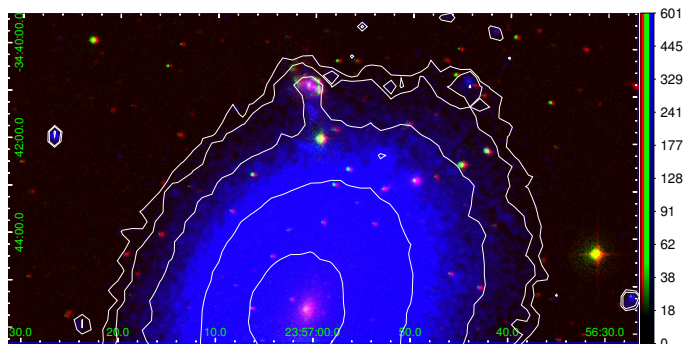


Fig. 11. RGB mosaic of the central-north part of A 4059. Red: optical filter (UK Schmidt telescope, public data). Green: UVM2 filter (OM instrument). Blue and contours: X-rays (EPIC MOS2+pn). The spiral galaxy ESO 349-G009 and the central cD galaxy are in the top and the bottom of the image respectively.

will mix more temperatures along the line of sight. A still broad range of temperatures in the local ICM beyond the core cannot be fully excluded, but seems more unlikely. Indeed, although the few outer local colder or hotter cells found in the kT residuals map (Fig. 8 top-right) might argue in favour of this second explanation, the temperature (and thus σ_T) measurements in the outer map cells are very sensitive to the background modelling, and are thus affected by these additional systematic uncertainties.

8. Conclusions

In this paper we have studied a very deep XMM-Newton observation (~ 140 ks of net exposure time) of the nearby cool-core cluster A 4059. Several temperature and abundance parameters

have been derived from the spectra both in the core and in 8 concentric annuli; moreover we were able to derive kT , σ_T and Fe abundance maps. We conclude the following:

- The temperature structure shows the cool-core and in addition increasing deviations from apparent isothermality in and out of the core.
- The abundances of O, Ne, Si, S, Ar, Ca and Fe all are peaked toward the core, and we report the presence of Fe and O beyond ~ 0.3 Mpc from the core. This suggests that the enrichment from SNIa and SNcc started early on in the cluster formation, probably through galactic winds in the young galaxy members.
- The EPIC image as well as the temperature and Fe abundance maps reveal strong asymmetries in the cluster core. We confirm a colder and Fe-richer ridge southwest of the core, previously found by *Chandra*, perhaps due to an intense ram-pressure stripping event. Therefore, in addition to an enrichment through galactic winds, ram-pressure stripping should have played more recently an important role in the inner core.
- The Ca/Fe abundance ratio in the core is particularly high (1.45 ± 0.14 using a combined EPIC fit), even accounting for systematic uncertainties. If we assume the Ca/Fe abundance of the entire core to be genuine, it is unlikely explained by current standard SNe yields models. Recently proposed ‘calcium-rich gap transient’ SNIa might be an interesting alternative to explain the high Ca abundance generally found in the ICM.
- Because of cross-calibration issues, the EPIC MOS and pn detectors measure significantly different values of temperature and most abundances. Although this leads to systematic uncertainties on their absolute values, the discrepancies are generally smaller when considering abundances relative to Fe. Moreover, it should not affect relative differences between spectra from different regions if use the same instrument(s). Fitting a Gaussian line and a local continuum instead of CIE models is a robust method to measure more reliable abundances.

Acknowledgements. This work is a part of the CHEERS (CHEmical Evolution Rgs cluster Sample) collaboration. We would like to thank its members and the anonymous referee for their feedback and discussions. FM thanks Huub Röttgering and Darko Donevski for useful discussions. LL acknowledges support by the DFG through grant LO 2009/1-1. YYZ acknowledges support by the German BMWi through the Verbundforschung under grant 50 OR 1304. This work is based on observations obtained with XMM-Newton, an ESA science mission with instruments and contributions directly funded by ESA member states and the USA (NASA). The SRON Netherlands Institute for Space Research is supported financially by NWO, the Netherlands Organisation for Space Research.

References

- Andernach, H., Tago, E., Einasto, M., Einasto, J., & Jaaniste, J. 2005, in *Astronomical Society of the Pacific Conference Series*, Vol. 329, *Nearby Large-Scale Structures and the Zone of Avoidance*, ed. A. P. Fairall & P. A. Woudt, 283–287
- Badenes, C., Borkowski, K. J., Hughes, J. P., Hwang, U., & Bravo, E. 2006, *ApJ*, 645, 1373
- Baumgartner, V. & Breitschwerdt, D. 2009, *Astronomische Nachrichten*, 330, 898
- Cash, W. 1979, *ApJ*, 228, 939
- Cattaneo, A. & Teyssier, R. 2007, *MNRAS*, 376, 1547
- Choi, Y.-Y., Reynolds, C. S., Heinz, S., et al. 2004, *ApJ*, 606, 185
- De Grandi, S., Santos, J. S., Nonino, M., et al. 2014, *A&A*, 567, A102
- De Luca, A. & Molendi, S. 2004, *A&A*, 419, 837
- de Plaa, J. 2013, *Astronomische Nachrichten*, 334, 416
- de Plaa, J., Werner, N., Bleeker, J. A. M., et al. 2007, *A&A*, 465, 345
- de Plaa, J., Werner, N., Bykov, A. M., et al. 2006, *A&A*, 452, 397
- De Young, D. S. 1978, *ApJ*, 223, 47
- Diehl, S. & Statler, T. S. 2006, *MNRAS*, 368, 497
- Frank, K. A., Peterson, J. R., Andersson, K., Fabian, A. C., & Sanders, J. S. 2013, *ApJ*, 764, 46
- Gnedin, N. Y. 1998, *MNRAS*, 294, 407
- Gunn, J. E. & Gott, III, J. R. 1972, *ApJ*, 176, 1
- Heinz, S., Choi, Y.-Y., Reynolds, C. S., & Begelman, M. C. 2002, *ApJ*, 569, L79
- Hickox, R. C. & Markevitch, M. 2006, *ApJ*, 645, 95
- Hopkins, A. M. & Beacom, J. F. 2006, *ApJ*, 651, 142
- Huang, Z. & Sarazin, C. L. 1998, *ApJ*, 496, 728
- Iakubovskiy, D. 2013, PhD thesis
- Ichinohe, Y., Werner, N., Simionescu, A., et al. 2014, *ArXiv e-prints*
- Iwamoto, K., Brachwitz, F., Nomoto, K., et al. 1999, *ApJS*, 125, 439
- Jansen, F., Lumb, D., Altieri, B., et al. 2001, *A&A*, 365, L1
- Kaastra, J. S., Ferrigno, C., Tamura, T., et al. 2001, *A&A*, 365, L99
- Kaastra, J. S., Mewe, R., & Nieuwenhuijzen, H. 1996, in *UV and X-ray Spectroscopy of Astrophysical and Laboratory Plasmas*, ed. K. Yamashita & T. Watanabe, 411–414
- Kaastra, J. S., Tamura, T., Peterson, J. R., et al. 2004, *A&A*, 413, 415
- Kapferer, W., Knapp, A., Schindler, S., Kimeswenger, S., & van Kampen, E. 2005, *A&A*, 438, 87
- Kuntz, K. D. & Snowden, S. L. 2008, *ApJ*, 674, 209
- Leccardi, A. & Molendi, S. 2008, *A&A*, 487, 461
- Lehmer, B. D., Xue, Y. Q., Brandt, W. N., et al. 2012, *ApJ*, 752, 46
- Lodders, K., Palme, H., & Gail, H.-P. 2009, *Landolt Börnstein*, 44
- Lovisari, L., Schindler, S., & Kapferer, W. 2011, *A&A*, 528, A60
- Matsushita, K. 2011, *A&A*, 527, A134
- Million, E. T., Werner, N., Simionescu, A., & Allen, S. W. 2011, *MNRAS*, 418, 2744
- Mitchell, R. J., Culhane, J. L., Davison, P. J. N., & Ives, J. C. 1976, *MNRAS*, 175, 29P
- Miyaji, T., Griffiths, R. E., Lumb, D., Sarajedini, V., & Siddiqui, H. 2003, *Astronomische Nachrichten*, 324, 24
- Moretti, A., Pagani, C., Cusumano, G., et al. 2009, *A&A*, 493, 501
- Moretti, A., Portinari, L., & Chiosi, C. 2003, *A&A*, 408, 431
- Mulchaey, J. S., Kasliwal, M. M., & Kollmeier, J. A. 2014, *ApJ*, 780, L34
- Mushotzky, R., Loewenstein, M., Arnaud, K. A., et al. 1996, *ApJ*, 466, 686
- Nomoto, K., Tominaga, N., Umeda, H., Kobayashi, C., & Maeda, K. 2006, *Nuclear Physics A*, 777, 424
- Ohashi, T. 1995, in *American Institute of Physics Conference Series*, Vol. 336, *Dark Matter*, ed. S. S. Holt & C. L. Bennett, 255–263
- Paterno-Mahler, R., Blanton, E. L., Randall, S. W., & Clarke, T. E. 2013, *ApJ*, 773, 114
- Peterson, J. R., Kahn, S. M., Paerels, F. B. S., et al. 2003, *ApJ*, 590, 207
- Peterson, J. R., Paerels, F. B. S., Kaastra, J. S., et al. 2001, *A&A*, 365, L104
- Pinto, C., Sanders, J. S., Werner, N., et al. 2014, submitted
- Read, A. M., Guainazzi, M., & Sembay, S. 2014, *A&A*, 564, A75
- Reiprich, T. H. & Böhringer, H. 2002, *ApJ*, 567, 716
- Reynolds, C. S., Casper, E. A., & Heinz, S. 2008, *ApJ*, 679, 1181
- Sato, K., Yamasaki, N. Y., Ishida, M., et al. 2007, *PASJ*, 59, 299
- Schellenberger, G., Reiprich, T. H., Lovisari, L., Nevalainen, J., & David, L. 2014, *ArXiv e-prints*
- Schindler, S., Kapferer, W., Domainko, W., et al. 2005, *A&A*, 435, L25
- Simionescu, A., Roediger, E., Nulsen, P. E. J., et al. 2009a, *A&A*, 495, 721
- Simionescu, A., Werner, N., Böhringer, H., et al. 2009b, *A&A*, 493, 409
- Simionescu, A., Werner, N., Finoguenov, A., Böhringer, H., & Brüggen, M. 2008, *A&A*, 482, 97
- Simionescu, A., Werner, N., Forman, W. R., et al. 2010, *MNRAS*, 405, 91
- Snowden, S. L. & Kuntz, K. D. 2013, *XMM ESAS cookbook*
- Tamura, T., Bleeker, J. A. M., Kaastra, J. S., Ferrigno, C., & Molendi, S. 2001, *A&A*, 379, 107
- Tamura, T., Kaastra, J. S., den Herder, J. W. A., Bleeker, J. A. M., & Peterson, J. R. 2004, *A&A*, 420, 135
- Tamura, T., Maeda, Y., Mitsuda, K., et al. 2009, *ApJ*, 705, L62
- Werner, N., de Plaa, J., Kaastra, J. S., et al. 2006, *A&A*, 449, 475
- Werner, N., Urban, O., Simionescu, A., & Allen, S. W. 2013, *Nature*, 502, 656
- Willingale, R., Starling, R. L. C., Beardmore, A. P., Tanvir, N. R., & O’Brien, P. T. 2013, *MNRAS*, 431, 394
- Zhang, Y.-Y., Andernach, H., Caretta, C. A., et al. 2011, *A&A*, 526, A105
- Zhang, Y.-Y., Reiprich, T. H., Finoguenov, A., Hudson, D. S., & Sarazin, C. L. 2009, *ApJ*, 699, 1178

Appendix A: Detailed data reduction

Appendix A.1: GTI filtering

In order to reduce the soft-proton (SP) background, we build Good Time Intervals (GTI) using the light-curves in the 10–12 keV band for MOS and 12–14 keV band for pn. We fit the count-rate histograms from the light curves of each instrument, binned in 100 s intervals, with a Poissonian function and we reject all time bins for which the number of counts lies outside the interval $\mu \pm 2\sigma$ (i.e. $\mu \pm 2\sqrt{\mu}$), where μ is the fitted average of the distribution. We repeat the same screening procedure and threshold (so-called 2σ -clipping) for 10 s binned histograms in the 0.3–10 keV band since De Luca & Molendi (2004) reported episodes of particularly soft background flares. In order to get a qualitative estimation of the residual SP flare contamination, we use the `Fin_over_Fout` algorithm which compares the count rates in and out of the FoV of each detector (De Luca & Molendi 2004). We found that in both observations MOS 1 displays a $F_{\text{in}}/F_{\text{out}}$ ratio higher than 1.3, meaning that the observations have been significantly contaminated by SP events. This value is still reasonable though, and a look at the filtered light curve lead us to safely keeping the MOS 1 datasets. Furthermore, a careful modelling of convenient SP spectral components are used in our spectral fittings as well (see Appendix B).

Appendix A.2: Resolved point sources excision

The point sources in our FoV contribute to the total flux and may bias the astrophysical results we aim to derive from the cluster emission. Therefore, they should be discarded. We detect all the resolved point sources (RPS) with the SAS task `edetect_chain` and we proceed a second check by eye in order to discard erroneous detections and possibly include a few missing candidates. It is common practice in extended source analysis to excise bright point sources from the EPIC data. Note however that a lot of sources have fluxes below the detection limit S_{cut} and an unresolved component might remain (Appendix B.2).

A remaining problem is how to choose the excision radius in an optimal way. A very small excision radius may leave residual flux from the excised point sources while a very large radius may cut out a significant fraction of the cluster emission leading to decreased S/N . Let us define A_{eff} as the extraction region area for the cluster emission when the point sources are excised with a radius r_s :

$$A_{\text{eff}} = A \left(1 - \pi r_s^2 \int_{S_{\text{cut}}}^{\infty} \left(\frac{dN}{dS} \right) dS \right) \quad (\text{A.1})$$

where N is the number of sources, S is the flux and A is the full detection area.

Since we are dealing with a Poissonian process, S/N can be estimated as: $S/N = \frac{C}{\sqrt{C+B}}$ where C and B are the number of counts of the cluster emission and the total background respectively. C depends on the extraction area and can thus be written $C = C^* A_{\text{eff}}$ where C^* is the local surface brightness of the cluster (counts/"). B can be divided into the instrumental or hard particle (HP) background I , an unresolved point sources (UPS) component and the remaining excised point source flux outside the excision region. The total background can be thus written as

$$B = I + \int_0^{S_{\text{cut}}} S \left(\frac{dN}{dS} \right) dS + (1 - EEF(r_s)) \int_{S_{\text{cut}}}^{\infty} S \left(\frac{dN}{dS} \right) dS \quad (\text{A.2})$$

where $EEF(r_s)$ is the encircled energy fraction of the PSF as a function of radius. We can finally write the total S/N as

$$S/N = \frac{C^* \sqrt{A \left(1 - \pi r_s^2 \int_{S_{\text{cut}}}^{\infty} \left(\frac{dN}{dS} \right) dS \right)}}{\sqrt{C^* + I + \int_0^{S_{\text{cut}}} S \left(\frac{dN}{dS} \right) dS + (1 - EEF(r_s)) \int_{S_{\text{cut}}}^{\infty} S \left(\frac{dN}{dS} \right) dS}} \quad (\text{A.3})$$

The optimum S/N can be then computed as a function of r_s and S_{cut} (Eq. A.3). In Appendix B.2 we discuss the origin of dN/dS . We find and adopt an optimised radius for RPS excision in our dataset of $\sim 10''$.

Appendix A.3: RGS spectral broadening correction from MOS 1 image

Because the RGS spectrometers are slitless and the source is spatially extended in the dispersion direction, the RGS spectra are broadened. The effect of the broadening of a spectrum by the spatial extent of the source is given by

$$\Delta\lambda = \frac{0.138}{m} \Delta\theta \text{Å} \quad (\text{A.4})$$

where m is the spectral order and θ is the offset angle in arcmin (see the XMM-Newton Users Handbook).

The MOS 1 DET Y direction is parallel to the RGS dispersion direction. Therefore, we extract the brightness profile of the source in the dispersion direction from the MOS 1 image and use this to account for the broadening following the method described by Tamura et al. (2004). This method is implemented through the `Rgsvprof` task in SPEX. As an input of this task, we choose a width of $10'$ around the core and along the dispersion axis, in which the cumulative brightness profile is estimated. In order to correct for continuum and background, we use a MOS 1 image extracted within 0.5–1.8 keV (i.e. the RGS energy band). This procedure is applied to both observations and we average the two spatial profiles obtaining a single profile that will be used for the stacked RGS spectrum.

Appendix B: EPIC background modelling

We split the total EPIC background into two categories, divided further into several components:

1. Astrophysical X-ray background, from the emission of astrophysical sources and thus folded by the response files. The AXB includes the Local Hot Bubble (LHB), the Galactic Thermal Emission (GTE) and the UPS.
2. Non-X-ray background (NXB), consisting of soft or hard particles hitting the CCD chips and being accounted as photon events. For this reason, they are *not* folded by the response files. The NXB contains the SP and the HP backgrounds.

In total five components are thus carefully modelled.

Appendix B.1: Hard Particle background

High energy particles are able to reach the EPIC detectors from every direction, even when the filter wheel is closed. Besides continuum emission, they also produce instrumental fluorescence lines which should be carefully modelled. Moreover, for low S/N areas, we observe a soft tail in the spectra due to the

Table B.1. Best-fit parameters of the HP component, estimated from the full FoV of FWC observations. An equal sign (=) means that the MOS 2 value is coupled with the MOS 1 one.

| Parameters | MOS 1 | MOS 2 | pn |
|---------------------------|------------------|-----------------|------------------|
| Y (10^{46} ph/s/keV) | 87.3 ± 1.2 | 133.6 ± 1.6 | 478 ± 117 |
| Γ | 0.33 ± 0.01 | = | 1.37 ± 0.70 |
| $\Delta\Gamma$ | -0.18 ± 0.02 | = | -1.08 ± 0.25 |
| E_{break} (keV) | 3.49 ± 0.25 | = | 1.05 ± 0.53 |
| b | ≤ 0.01 | = | 0.39 ± 0.17 |

Table B.2. Fluorescent instrumental lines produced by the hard particles. The centroid energies are adapted from Snowden & Kuntz (2013) and Jakubovskiy (2013) (MOS except Si K) and from our best-fit model (pn + MOS Si K).

| MOS | | pn | |
|--------------|---------------|--------------|---------------|
| Energy (keV) | Line | Energy (keV) | Line |
| 1.49 | Al K α | 1.48 | Al K α |
| 1.75 | Si K α | 4.51 | Ti K α |
| 5.41 | Cr K α | 5.42 | Cr K α |
| 5.90 | Mn K α | 6.35 | Fe K α |
| 6.40 | Fe K α | 7.47 | Ni K α |
| 7.48 | Ni K α | 8.04 | Cu K α |
| 8.64 | Zn K α | 8.60 | Zn K α |
| 9.71 | Au L α | 8.90 | Cu K β |
| | | 9.57 | Zn K β |

intrinsic noise of the detector chips. A good estimate of the HP background can be obtained by using Filter Wheel Closed (FWC) data which are publicly available on the XMM-Newton SOC webpage⁵. We select FWC data that were taken on 1 October 2011 and 28 April 2011 with an exposure time of 53.7 ks and 35.5 ks for MOS and pn respectively. We removed the MOS 1 events from CCD3, CCD4 and CCD6 to be consistent with our current dataset.

Instead of subtracting directly the FWC events from our observed spectra, modelling directly the HP background allows a much more precise estimate of the instrumental lines fluxes, which are known to vary across the detector (Snowden & Kuntz 2013).

We fit the individual FWC MOS and pn continuum spectra with a broken power-law $F(E) = YE^{-\Gamma}e^{\eta(E)}$ where $\eta(E)$ is given by

$$\eta(E) = \frac{r\xi + \sqrt{r^2\xi^2 + b^2(1-r^2)}}{1-r^2} \quad (\text{B.1})$$

with $\xi = \ln(E/E_0)$ and $r = \frac{\sqrt{1+(\Delta\Gamma)^2}-1}{|\Delta\Gamma|}$ (see SPEX manual). In this model, the independent parameters are A , Γ (spectra index), $\Delta\Gamma$ (spectral index break), E_0 (break energy) and b (break strength). Unlike the instrumental lines, this continuum does not vary strongly across the detector. Tables B.1 and B.2 show the best fit parameters that we found for the entire FoV extraction area and the modelled instrumental lines respectively. In addition to the broken power-law, each instrumental line is modelled with a narrow (FWHM ≤ 0.3) Gaussian function. Although a delta function is more realistic, in this case allowing a (slight) broadening optimises the correction for the energy redistribution on the instrumental lines.

⁵ <http://xmm.esac.esa.int>

Appendix B.2: Unresolved Point Sources

An important component of the EPIC background is the contribution of UPS to the total X-ray background. Its flux can be estimated using the so called $\log N$ – $\log S$ curve derived from blank field data. This curve describes how many sources are expected at a certain flux level. The source function has the form of a derivative (dN/dS) and can be integrated to estimate the number of sources in a certain flux range:

$$N(< S) = \int_S^\infty \left(\frac{dN'}{dS'} \right) dS' \quad (\text{B.2})$$

where N is the number of sources and S is the low-flux limit.

The most common bright UPS are AGNs, but also galaxies and hot stars contribute. Based on the *Chandra* deep field, Lehmer et al. (2012) find that AGNs are the most dominant in terms of number counts but in the 0.5–2 keV band the galaxy counts become higher than the AGN counts below a few times 10^{-28} W m⁻² deg⁻². The assumed spectral model of this component is a power-law with a photon index of $\Gamma=1.41$ (see e.g. Moretti et al. 2003; De Luca & Molendi 2004). In reality, the power-law index may vary slightly between 1.4–1.5, given the uncertainties in the different surveys and estimations (Moretti et al. 2009). Based on the *Chandra* Deep Field South (CDF-S) data, Lehmer et al. (2012) define the (dN/dS) relations for each source category as follows:

$$\frac{dN^{\text{AGN}}}{dS} = \begin{cases} K^{\text{AGN}}(S/S_{\text{ref}})^{-\beta_1^{\text{AGN}}} & (S \leq f_b^{\text{AGN}}) \\ K^{\text{AGN}}(f_b/S_{\text{ref}})^{\beta_2^{\text{AGN}}-\beta_1^{\text{AGN}}}(S/S_{\text{ref}})^{-\beta_2^{\text{AGN}}} & (S > f_b^{\text{AGN}}) \end{cases} \quad (\text{B.3})$$

$$\frac{dN^{\text{gal}}}{dS} = K^{\text{gal}}(S/S_{\text{ref}})^{-\beta^{\text{gal}}} \quad (\text{B.4})$$

$$\frac{dN^{\text{star}}}{dS} = K^{\text{star}}(S/S_{\text{ref}})^{-\beta^{\text{star}}} \quad (\text{B.5})$$

Each relation describes a power-law with a normalisation constant K and a slope β . Since the (dN/dS) relation of AGNs shows a break, there is an additional β_2 parameter and a break flux f_b . The reference flux is defined as $S_{\text{ref}} \equiv 10^{-14}$ erg cm⁻² s⁻¹. The best fit parameters for the studied energy bands are listed in Table 1 of Lehmer et al. (2012).

The relations above can be used to estimate the flux from sources that are not detected in our EPIC observations. The UPS component also holds for the deepest *Chandra* observations. Hickox & Markevitch (2006) found a detection limit of 1.4×10^{-16} in a 1 Ms CDF-S observation and estimated the unresolved flux to be $(3.4 \pm 1.7) \times 10^{-12}$ erg cm⁻² s⁻¹ deg⁻² in the 2–8 keV band. Since *Chandra* has a much lower confusion limit and a narrower PSF, we do not expect EPIC to reach this detection limit even in a deep cluster observation. It is therefore not necessary to know the $\log N$ – $\log S$ curve below this flux limit to obtain a reasonable estimate for the unresolved flux.

In the flux range from 1.4×10^{-16} up to the EPIC flux limit, we can calculate the flux using the $\log N$ – $\log S$ relation. The total unresolved flux Ω_{UPS} for the 2–8 keV band is then calculated using

$$\Omega_{\text{UPS}} = 3.4 \times 10^{-12} + \int_{1.4 \times 10^{-16}}^{S_{\text{cut}}} S' \left(\frac{dN}{dS'} \right) dS' \text{ erg cm}^{-2} \text{ s}^{-1} \text{ deg}^{-2}.$$

(B.6)

Using the Eqs. B.3, B.4 and B.5 for $\frac{dN}{dS}$ in the integral above, the unresolved flux calculation is straightforward. Given the detection limit of our observations $S_{\text{cut}} = 3.83 \times 10^{-15} \text{ W m}^{-2}$, we find a total UPS flux of $8.07 \times 10^{-15} \text{ W m}^{-2} \text{ deg}^{-2}$. This value can be used to constrain the normalisation of the power-law component describing the AXB background in cluster spectral fits. Note that this method does not take the cosmic variance into account (see e.g. Miyaji et al. 2003), which means that the normalisation may still be slightly biased.

Appendix B.3: Local Hot Bubble and Galactic Thermal Emission

The LHB component is thought to originate from a shock region between the solar wind and our local interstellar medium (Kuntz & Snowden 2008), while the GTE is the X-ray thermal emission from the Milky Way halo. At soft energies (below ~ 1 keV), the flux of those two foreground components is significant. They are both known to vary spatially across the sky but we assume they do not change significantly within the EPIC FoV. Both components are modelled with a *CIE* component where we assume the abundances to be proto-solar. Both temperatures are left free but are expected to be within 0.1–0.7 keV. The GTE component is absorbed by a gas with hydrogen column density ($N_H = 1.26 \times 10^{20} \text{ cm}^{-2}$) while the LHB component is not.

Appendix B.4: Residual Soft-Proton component

Even after having filtered soft flares events from our raw datasets, there remains a quiescent level of SP that might affect the spectra, especially at low S/N and above ~ 1 keV. It is extremely hard to precisely estimate the normalisation and the shape of its spectrum since SP quiescent events strongly vary with detector position and time (Snowden & Kuntz 2013). They may also depend on the attitude of the satellite. For these reasons, blank sky XMM-Newton observations are not good enough for our deep exposures. The safest way to deal with this issue is to model its spectrum by a single power-law (Snowden & Kuntz 2013). Using a broken power-law might be slightly more realistic, but the number of free parameters is then too high to make the fits stable. Although the spectral index Γ of the power-law is unfortunately unpredictable and may be different for MOS and pn instruments as well as between different observations. Since Snowden & Kuntz (2013) reported spectral indices between ~ 0.1 – 1.4 , we allow the Γ parameter in our fits varying within this range.

Appendix B.5: Application to our datasets

We apply the procedure described above for each component on our two observations of A4059. We extract an annular region with inner and outer radii of $6'$ and $12'$ respectively and centred on the cluster core (Fig. 1, the two outermost annuli), assuming that all the background components described above contribute to the detected events covered by this area. In order to get a better estimation of the foreground thermal emission (GTE & LHB), we fit a ROSAT PSPC spectrum from Zhang et al. (2011) simultaneously with our EPIC spectra. This additional observation covers an annulus centred to the core and with inner and outer radii of $28'$ ($\sim r_{200}$) and $40'$ ($\sim r_{200} + 12'$) respectively, avoiding instrumental features and visible sources. Note that in this fit we also take the UPS contribution into account. Depending on

Table B.3. Best-fit parameters values of the total background estimated in the $6'$ – $12'$ annular region around the core (see text). A simple asterisk (*) means that the value reaches the upper or lower fixed range. An equal sign (=) means that the corresponding parameters from DO#1 and DO#2 are coupled together.

| Bkg comp. | Parameter | Instrument | DO#1 | DO#2 |
|-----------|----------------------------------|------------|-------------------|--------------------------|
| SP | Norm. (10^{46} ph/s/keV) | MOS 1 | 46 ± 10 | 30.3 ± 4.5 |
| | | MOS 2 | 18.1 ± 9.4 | 14.5 ± 3.4 |
| | | pn | 22.8 ± 4.2 | 15.70 ± 1.07 |
| | Γ | MOS | 1.18 ± 0.08 | 1.63 ± 0.11 |
| | | pn | 0.29 ± 0.09 | $0.10 \pm_{0.00}^{0.02}$ |
| GTE | Y (10^{69} m^{-3}) | MOS+pn | 26.4 ± 4.7 | = |
| | kT (keV) | | 0.54 ± 0.08 | = |
| LHB | Y (10^{69} m^{-3}) | MOS+pn | 311.8 ± 5.1 | = |
| | kT (keV) | | 0.168 ± 0.002 | = |
| UPS | Norm. (10^{49} ph/s/keV) | MOS+pn | 58.29 (fixed) | = |
| | Γ | | 1.41 (fixed) | = |

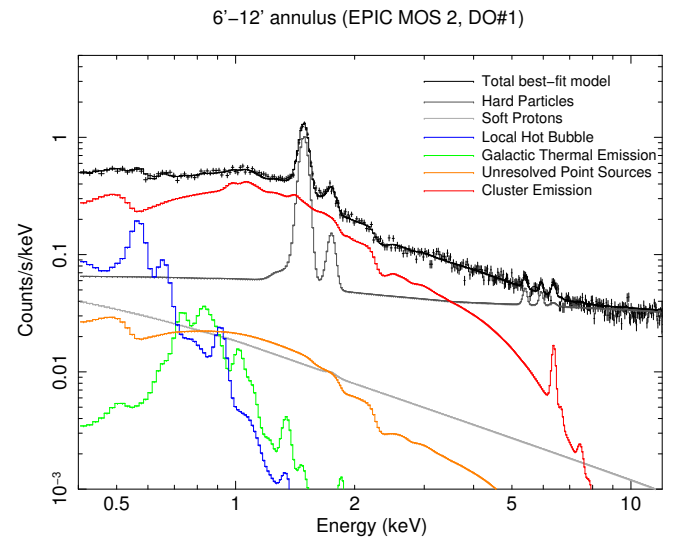


Fig. B.1. EPIC MOS2 spectrum of the $6'$ – $12'$ annular region around the core (see text). The black solid line represents the total best fit model. Its individual modelled components (background and cluster emission, colored solid lines) are also shown.

the extraction area, all the normalisations (except for the UPS component, Appendix B.2) are left free but properly coupled between each observation and instrument.

Table B.3 shows the different background values that we found for the extracted annulus. Fig. B.1 shows the result for the MOS 2 spectrum at the first observation, its best fit model as well as the contribution of every modelled component. As expected, the NXB contribution is more important at high energies. Above ~ 5 keV, the cluster emission is much smaller than the HP background. Consequently and as already reported, the temperature and abundances measured by EPIC are harder to estimate in the outer parts of the FoV.

Finally we apply and adapt our best background model to the core region (Sect. 4) and the 8 concentric annuli (Sect. 5). The normalisation of every background component has been scaled and corrected for vignetting if necessary. From the background parameters, only the normalisations of the HP component (initially evaluated from the 10–12 keV band, where negligible cluster emission is expected), as well as those of the instrumental fluorescent lines, are kept free for all the spectra. In the outermost annulus ($9'$ – $12'$) we ignore the channels below 0.4 keV (MOS) and 0.6 keV (pn) to avoid low energy instrumental noise. For

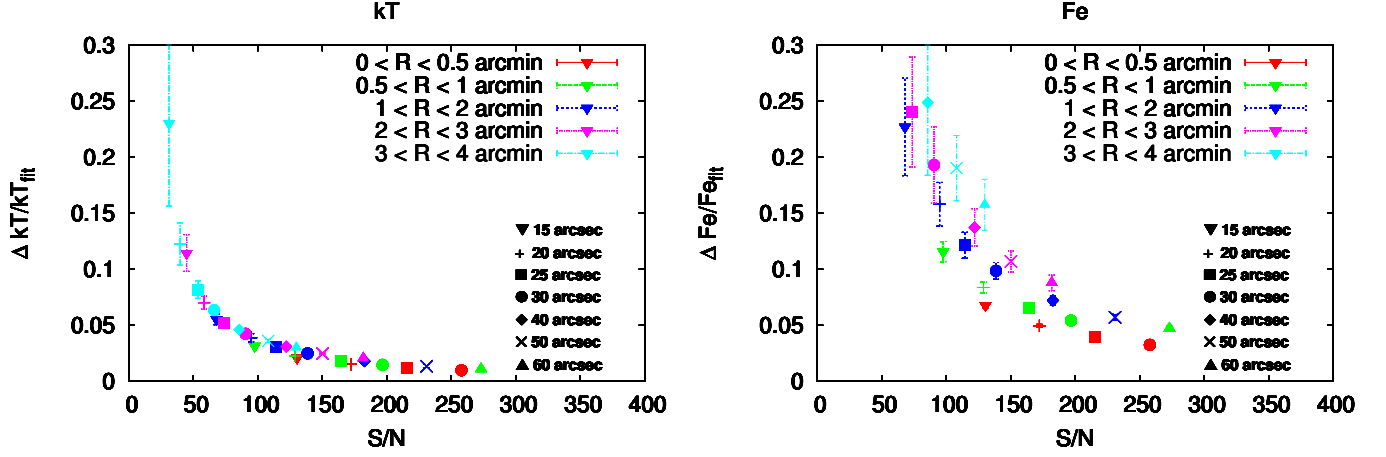


Fig. B.2. Expected relative errors on the temperatures and abundances. Different cell sizes (symbols) are simulated within the 5 innermost annuli (colors).

the same reason we ignore the channels below 0.4 keV (MOS) and 0.5 keV (pn) in the second outermost annulus (6'–9'). The background is also applied to and adapted for the analysis of the spectra of each map cell (Sect. 6).

Appendix C: S/N requirement for the maps

Despite their good statistics, we want to optimise the use of our data and find the best compromise between the required spatial resolution of our maps (Sect. 6) and S/N . The former is necessary when searching for inhomogeneities and kT /metal clumps (i.e. the smaller the better), the latter to ensure that the associate error bars are small enough to make our measurement significant. Clearly, these variables depend on the properties of the cluster and on the exposure time of our observations.

We perform a set of simulations to determine what the best combination of S/N and spatial resolution is for the case of A4059. For every annulus (i.e. the ones determined in Sect. 5) we simulate a spectrum with input parameters (i.e. kT , O, Ne, Mg, Si, S, Ca, Fe, Ni, and the normalisation) corresponding to the ones determined in the radial profiles analysis. The AXB and the HP background are added to the total spectrum by using the properties derived in Appendix B. We allow their respective normalisations to vary within $\pm 3\%$ in order to take into account spatial variations on the FoV. Starting from what we derived for the radial profile, we rescale the normalisation of the simulated spectrum to the particular spatial resolutions we are interested (here we test 15'', 20'', 25'', 30'', 40'', 50'' and 60''). We then fit the spectrum as done for the real data and for all the annuli and spatial resolutions we calculate the relative errors on the temperature and Fe abundance in a function of S/N . The median values of 300 realisations are shown in Fig. B.2, as well as their 1σ errors.

A S/N of 100 is required to measure the abundance with a relative error lower than $\sim 20\%$. With such a choice the temperature will be also determined with a very good accuracy (relative errors always lower than $\sim 5\%$).